Earth-Science Reviews 258 (2024) 104962

Contents lists available at ScienceDirect

Earth-Science Reviews

journal homepage: www.elsevier.com/locate/earscirev

Review Article

Seismic cyclostratigraphy: Hypothesis testing for orbital cyclicity using seismic reflection data

Jonathan Ford [a,*], Angelo Camerlenghi [a], Michele Rebesco [a], Gabriele Uenzelmann-Neben [b], Estella Weigelt [b]

[a] Istituto Nazionale di Oceanografia e di Geofisica Sperimentale – OGS, Trieste, Italy
[b] Alfred-Wegener-Institut, Helmholtz-Zentrum für Polar-und Meeresforschung, Bremerhaven, Germany

ARTICLE INFO

Keywords:
Milanković cycles
Seismic reflection imaging
Ocean drilling
Monte Carlo simulation

ABSTRACT

Several studies report observations of orbital cyclicity in seismic reflection data as distinct power spectral peaks that align with Milanković periodicities. It remains unclear, however, if hypothesis testing for orbital forcing using seismic data can be performed with statistical power comparable to directly sampled data, such as outcrop, drill core or borehole logs. In this study we aim to quantify this using Monte Carlo ensemble modelling to compare seismic and borehole log cyclostratigraphy. We develop a method for spectral background estimation that accounts for some of the amplitude and frequency effects inherent to seismic data. We then forward model the seismic response of an ensemble of models where the acoustic impedance approximates red noise, with and without an injected orbital signal from an astronomical solution. We demonstrate two examples: i) a simplified model with constant background velocity, constant sedimentation rate and a parametric seismic source wavelet, and ii) a real-world example based on ODP Site 1084 (Cape Basin). We observe that the sensitivity and specificity for the seismic case are strongly frequency-dependent, compared to the largely frequency-independent results for the borehole log cyclostratigraphy. For the real-world data example, we observe a spectral peak corresponding to 95 kyr eccentricity cyclicity with an uncalibrated confidence level of >95 %. Our Monte Carlo ensemble modelling, however, shows that the false positive rate at this frequency and confidence level is around 25 %, compared to around 5 % for the equivalent borehole log cyclostratigraphy. We also demonstrate short-period eccentricity modulation and bundling analysis applied to the seismic data, which is able to successfully invert for the model sedimentation rate for the simplified synthetic example. These results suggest that reliably identifying Milanković cycles from seismic reflection data is strongly dependent on the site geology, the geophysical parameters and the spectral frequency in question. Seismic examples should ideally be "ground truthed" against positive evidence of orbital cyclicity from a nearby borehole. In such cases, seismic data can be used to extrapolate borehole cyclostratigraphy data both laterally between boreholes and vertically beyond the maximum drilled depth. We suggest that sediment drifts are the sedimentary environment that is most promising for the detection of orbital cyclicity in seismic reflection images, and similar principles could also be applied to other geophysical reflection methods such as sub-bottom profilers.

1. Introduction

Cyclostratigraphic methods have been widely applied to calibrate geological timescales and to better understand the paleoclimate response to orbitally-forced insolation, primarily based on directly sampled paleoclimate proxy data from outcrop exposures, drill core or borehole logs (Hays et al., 1976; Hinnov, 2013; Zeeden et al., 2023). Most such methods are based on spectral analysis of time-series data within a stratigraphic interval, where quasi-periodic orbital forcing (Milanković cycles) might be identified as distinct peaks in the power spectrum, either by their amplitude above a background noise floor (Vaughan et al., 2011; Weedon, 2003), by the frequency ratio between peaks (Meyers and Sageman, 2007), or by their amplitude relationship (Meyers, 2015, 2019). Beyond directly sampled data, a handful of studies also claim to observe orbital cyclicity in the power spectra of seismic reflection data (e.g., Weigelt and Uenzelmann-Neben, 2007;

* Corresponding author.
E-mail address: jford@ogs.it (J. Ford).

https://doi.org/10.1016/j.earscirev.2024.104962
Received 10 March 2024; Received in revised form 15 October 2024; Accepted 16 October 2024
Available online 20 October 2024

Horn and Uenzelmann-Neben, 2016; Rebesco et al., 2021), although the validity of such approaches under real-world geological conditions and geophysical constraints has been questioned (Mitchell, 2016). More problematically, these studies simply identify distinct spectral peaks that appear to correspond to the expected periodicity of major Milanković cycles, without attempting to estimate their statistical significance. This leaves open the possibility that these apparent detections of orbital cyclicity from seismic data could, in reality, represent false positives.

A common goal of cyclostratigraphy is to discriminate between spectral peaks that truly represent orbital forcing and spurious peaks caused by background noise. The magnitude and spectral character of the preserved orbital signal strongly depends on the response of the depositional environment to orbital forcing; post-depositional disturbance such as compaction and bioturbation; and spectral distortion introduced in converting from stratigraphic depth (or equivalently seismic two-way traveltime; TWTT) to geological age (Hilgen et al., 2015). Here background noise includes both sedimentation uncorrelated with orbital forcing and spectral contamination introduced by the sampling strategy and the subsequent spectral transform, both of which can induce spurious spectral peaks (Meyers, 2019). Faced with the difficulty of conclusively identifying orbital cyclicity from power spectra, workers in the field of cyclostratigraphy have developed a range of statistical procedures that instead quantify the likelihood that a particular spectral peak is caused by orbital forcing (e.g., Huybers and Wunsch, 2005; Meyers, 2015; Meyers and Malinverno, 2018). These so-called hypothesis testing approaches first posit the null hypothesis that orbital cyclicity is *not* preserved within a stratigraphic interval. The presence of an orbital signal is confirmed by refuting the null hypothesis at a given confidence level, usually by showing that the amplitude of a spectral peak exceeds the background noise floor by a given factor. The probability that the experiment will correctly reject the null hypothesis is termed the sensitivity (i.e., the probability that orbital cyclicity is detected when it is preserved). The specificity of the test is the probability that the experiment will correctly accept the null hypothesis (i.e., the probability that orbital cyclicity is not detected when it is not preserved). An ideal test with high discriminatory power will have both high sensitivity (high true detection rate) and a high specificity (low false detection rate). There is a general consensus in the cyclostratigraphy literature that workers should prioritise minimising false detections (Type I errors), the logic being that, as the preservation of orbital cyclicity requires very specific geological conditions, cyclic stratigraphy should be relatively rare; detecting orbital forcing when in fact it is not preserved is misleading and more dangerous than failing to detect orbital forcing when it is preserved (Type II errors) (Vaughan et al., 2011). In practice, increasing the specificity of a statistical test by increasing the confidence level will generally decrease the sensitivity, which limits the real-world scenarios where cyclostratigraphy can be successfully applied (Weedon, 2022).

The relationship between the confidence level and the discriminatory power of a particular hypothesis testing approach can be empirically calibrated using Monte Carlo ensemble modelling (Meyers, 2012; Vaughan et al., 2011). This involves generating models of sedimentary sequences with a randomly varying background sedimentary noise model, commonly AR(1) first-order autoregressive "red" noise (Mann and Lees, 1996). An ensemble of realisations are generated: the first half with background noise only, and the second half with background noise plus an orbital signal, usually assumed based on an astronomical solution (e.g., Laskar et al., 2004). The spectral peak detection and hypothesis testing method is applied to both ensemble halves, which gives true and false detection rates at all orbital periods. Previous workers have shown that for directly sampled time series the confidence level is equivalent to the inverse of the false detection rate (Vaughan et al., 2011; Meyers, 2012, 2019). In other words, if we set the confidence level to 95 %, we can expect that on average 5 % of the detections at a particular frequency will be in error. It should be noted that there is considerable debate in the literature about how to interpret these confidence intervals, with these numbers being strictly valid only for single frequency tests (Meyers, 2012; Vaughan et al., 2015; Weedon, 2022; Smith, 2023).Various corrections for multiple frequency tests are proposed in the literature, including for scenarios where we search the spectrum for orbital peaks or "tune" the power spectrum by varying the age-depth model without *a priori* knowledge of the presence of cyclicity (Abdi, 2007; Schulz and Mudelsee, 2002).

In this study we aim to understand if, under common geological and geophysical conditions, seismic reflection data are able to discriminate Milanković orbital cyclicity from background sedimentation. We use a Monte Carlo ensemble modelling approach to calibrate the sensitivity and specificity against the confidence level for both borehole and seismic cases. We first outline the theoretical basis by which cyclicity preserved in the subsurface acoustic impedance can be expressed in the power spectrum of the recorded seismic trace, and propose a method to estimate the spectral background and perform peak detection that accounts for the band-limited character of seismic data. We develop two synthetic models: i) a simplified example with constant sedimentation rate (approx. 1.7 Ma–present), no velocity gradient and a known seismic wavelet and ii) a more realistic example based on borehole and seismic data from ODP Site 1084, Cape Basin (offshore Namibia, approx. 4.6 Ma–present), with variable sedimentation rate, variable seismic velocity and a non-parametric, estimated seismic wavelet (Shipboard Scientific Party, 1998c). Based on the results of this modelling we examine the likelihood that the spectral peaks observed at this site are truly a result of orbital cyclicity as hypothesised in Weigelt and Uenzelmann-Neben (2007). We also demonstrate a practical application of seismic cyclostratigraphy by inverting for sedimentation rate using short-period eccentricity modulation and bundling analysis (TimeOpt), for both the simplified synthetic and Cape Basin cases. Finally we discuss the resulting limitations and possible future applications of seismic cyclostratigraphy and propose rules-of-thumb for scenarios in which it may be successfully applied to real-world data in the future.

2. Methodology

2.1. Expression of cyclicity in seismic reflection data

The seismic reflection response is primarily controlled by vertical changes in the acoustic impedance, Z, the product of the bulk density, ρ, and the seismic velocity, v. The normal-incidence reflectivity, r_0, is approximately the first derivative of the acoustic impedance (Pullammanappallil et al., 1997). After Claerbout (1985), we can approximate an idealised depth domain seismic trace, $y_0(z)$, as the convolution of a reflectivity series with the depth domain seismic wavelet, $w(z)$:

$$y_0(z) \approx r_0(z) * w(z) \tag{1}$$

$$\approx \frac{\partial}{\partial z} Z(z) * w(z). \tag{2}$$

This approximation models the vertical normal-incidence primary reflections only (no multiples or noise, zero source-receiver offset). According to convolution theorem, the Fourier transform of the convolution of two signals is equivalent to the product of their individual Fourier transforms. The derivative of a real signal in Fourier domain is equivalent to a multiplication by the independent variable, and the power spectrum of a signal is the square of the absolute Fourier transform. Together these mean that the power spectrum of the depth domain seismic trace, P_{y_0}, can be related to the power spectra of the impedance, P_Z, and the wavelet, P_w, by:

$$P_{y_0}(k_z) \approx k_z^2 P_Z(k_z) \cdot P_w(k_z), \tag{3}$$

where $k_z = 1/\lambda$ is the vertical wavenumber (spatial frequency), the in-

verse of the vertical wavelength (Irving and Holliger, 2010; Pullammanappallil et al., 1997).

Eq. 3 implies that if a periodic signal is expressed in the acoustic impedance, cyclicity will also be evident in the power spectrum of the depth domain seismic trace, if the bandwidth of the seismic wavelet includes the relevant spatial frequencies. Consequently, for orbital cyclicity to be expressed in the seismic trace, the cyclicity must first be preserved in the seismic velocity and/or the bulk density, and after conversion to depth domain (or equivalently age domain) the seismic bandwidth must include the relevant spatial (or temporal) frequencies of the orbital signal. In addition, the seismic reflection experiment introduces the following geophysical constraints:

1. Seismic sources are relatively narrow-band, typically on the order of 5 octaves (Sheriff and Geldart, 1995), compared to geological structure that is heterogeneous over a broad scale range (Levander et al., 1994; Holliger, 1996). The source frequency response is non-flat, typically having a dominant peak and often several secondary peaks and notches.
2. Seismic amplitudes are attenuated with propagation distance due to the expanding wavefront (geometrical spreading). High frequencies are preferentially attenuated (spectral reddening) and the phase of the wavelet is distorted with propagation distance (dispersion) due to absorption (Mavko et al., 1979).
3. Long-wavelength impedance variation is attenuated (spectral blueing) inversely proportional to the wavelength independent of the source bandwidth, as seismic images are sensitive to reflectivity, approximately the derivative of impedance (Eq. 3). This means that reflection data primarily image the fine-scale, short-wavelength (<100s of metres) subsurface structure (Poppeliers, 2007).
4. The seismic experiment contains additional sources of non-geological periodicity, e.g., reverberations from short-period multiples; the bubble pulse (in marine data); and “ghost reflections” from interference with the free surface, all of which could generate distinct but spurious spectral peaks. Real-world seismic images also contain noise inherent to the seismic experiment (environmental and acquisition noise) and additional noise generated by data processing and imaging (processing noise).

Even though seismic processing aims to compensate for the above limitations, the signal-to-noise ratio is invariably decreased and there is often frequency-dependent, non-stationary distortion of the amplitude and phase of the seismic wavelet at later arrival times. In addition, errors in the interval velocity model used to convert from TWTT (the natural recording domain of seismic data) to depth domain, and subsequently the depth-age model used to convert to stratigraphic age, will introduce distortion at long wavelengths. Compared to the power spectra of directly sampled data such as borehole logs or core-scanning data, the background noise floor of a seismic trace will be overall higher. As a result, spectral peaks in the power spectrum of a comparable seismic trace will inevitably be defocused—broader and lower amplitude with respect to the noise floor. Spectral peaks from cyclicity are generally already partially defocused in geology due to contamination and distortion during deposition and preservation (Meyers, 2019), geophysical reflection data will further amplify this effect.

2.2. Spectral background estimation

Statistical tests such as spectral background estimation and assigning corresponding confidence intervals can be used as a threshold to discriminate true cyclicity from background noise at a given confidence level (Meyers, 2019). In this study we follow a LOWSPEC-based (Locally-Weighted Regression Spectral Background Estimation) approach for spectral baseline fitting and significance testing (after Meyers, 2012). For a directly sampled paleoclimate proxy from drill core, borehole or outcrop this proceeds as:

1. Estimate the background spectral power using a parametric noise model, e.g., AR(1) red noise (Mann and Lees, 1996).
2. Whiten the spectrum by subtracting the estimated background noise model.
3. Estimate the spectral baseline, which should be close to flat after spectral whitening, by fitting a locally-weighted scatterplot smoothing (LOWESS) trend.
4. Define confidence levels above the spectral baseline using a chi-square distribution

Spectral peaks exceeding the desired confidence level are counted as detections (statistically significant peaks).

Compared to directly estimating the spectral baseline from the measured power spectrum (e.g., Mann and Lees, 1996), LOWSPEC is attractive because it is flexible in the choice of background noise model (such as higher-order autoregressive noise models, e.g., Sproson, 2020), and the use of a locally-weighted regression in the spectral baseline estimation allows for imperfect estimation and subtraction of the background noise in the spectral whitening step. This is especially relevant for the seismic case, where the reflectivity has effectively been filtered by the narrow-band and non-flat seismic wavelet (Section 2.1), meaning that estimating the background noise spectrum of a seismic trace is more challenging than for directly sampled data. Meyers (2012) and Weedon (2022) demonstrate, using Monte Carlo ensemble modelling, that if the background noise can be correctly estimated and removed, confidence levels are equivalent to the specificity (i.e., a given spectral peak above the 99 % significant level has a 1 % chance of being a false detection, on average). There has been extensive discussion in the literature about the true statistical meaning of these confidence levels, and under which circumstances they are valid (e.g., Vaughan et al., 2011; Meyers, 2019; Weedon, 2022; Smith, 2023). For this study, we do not enter this discussion, as we aim to instead simply compare borehole (direct sampling) and seismic cyclostratigraphic methods.

For the seismic case, we propose a modified LOWSPEC approach (Meyers, 2012) for spectral baseline estimation on the power spectra of seismic traces that have been transformed from TWTT to age domain. The major difference is in the spectral whitening step, in which we:

1. Estimate the seismic wavelet and remove its frequency-dependent amplitude filtering effect by deconvolving the wavelet from the seismic trace (using a water-level deconvolution procedure).
2. Correct for the preferential loss of low-wavenumber acoustic impedance information by multiplying the amplitude spectrum by the wavelength in Fourier domain (Eq. 3).
3. Estimate the AR(1) noise parameters (variance, S_0, and lag-1 autocorrelation coefficient, φ) and subtract the noise model in frequency domain to give the whitened spectrum.

We note that (1) will artificially boost the amplitudes of frequencies outside the seismic bandwidth, in effect amplifying the noise at these frequencies. This is not problematic, because the Monte Carlo ensemble modelling will (correctly) represent these frequencies as having high false positive rates. It should also be noted that (1) requires an estimate of the seismic wavelet: this could be recorded by a far-field hydrophone, modelled or simply estimated from the seafloor reflection in marine seismic data (as in this study). An amplitude correction for geometrical spreading should be applied to the data because ideally all parts of the analysed interval should contribute equally to the power spectral estimate, even as seismic amplitudes naturally decrease with increasing propagation distance (Section 2.1, Mitchell, 2016). Following the whitening step, we use a LOWESS regression to estimate the spectral baseline. The assigning of confidence intervals and peak detection proceeds as for the directly sampled data (Meyers, 2012).

2.3. Model building and synthetic modelling

We model the background sedimentary noise as an AR(1) random noise series, regularly sampled in age domain and parameterised by the red noise variable, φ, which controls the contribution of long wavelengths to the spectrum (redness). We then add an orbital signal in age domain with unit variance. Here we use an astronomical solution for insolation from Laskar et al. (2004), but in principle this could be any orbital signal. Using the age model, we interpolate to a series that is regularly sampled in depth domain. This depth domain series is subsequently scaled to match the desired statistical properties of, e.g., a velocity or density model.

For this study we model an acoustic impedance pseudo-borehole log, as it is the parameter most directly comparable to the seismic reflection trace. The method could also be applied to any borehole log (or derived pseudo-log) that measures a parameter relevant to acoustic impedance. To create the synthetic acoustic impedance pseudo-logs, we first model the synthetic sonic and density logs separately, to reflect the respective resolutions of the wireline logging tools used during ODP Leg 175 (Shipboard Scientific Party, 1998a). The synthetic sonic log is modelled by convolving a 3 m length boxcar window with the velocity series, to match the approximate vertical resolution of the Sonic Digital Tool (transmitter-receiver separation 2.4–3.6 m). Similarly, the synthetic density log is modelled by convolving a 0.3 m length boxcar window with the density series to match the approximate vertical resolution of the Hostile Environment Lithodensity Sonde (Ocean Drilling Program, 2004). The resulting logs are resampled to 0.15 m to match the sample interval used in ODP Leg 175 and multiplied together to produce the synthetic acoustic impedance pseudo-log. For real-world data, an acoustic impedance pseudo-log is generated simply by multiplying the measured sonic and density logs.

For the seismic modelling we use a 1-D visco-acoustic finite difference scheme (2nd order in time, 8th order in space) to forward model the zero-offset seismic reflection response, including the effects of multiples and frequency-dependent attenuation. The modelling scheme uses the 2nd order visco-acoustic wave equation based on the Standard Linear Solid (SLS) model for attenuation and dispersion (Carcione, 2014) and is implemented using Devito, an open-source Python library for finite difference modelling (Louboutin et al., 2019). The top edge of the model is a free surface and no absorbing boundary is used at the bottom edge of the model. Instead, the computational domain is padded at the bottom by a distance that is equivalent to the whole interval, to ensure reflections from grid boundaries are not recorded within the same time window as the primary reflections, as even small reflections from imperfect absorbing boundaries are liable to strongly affect the resulting spectrum. The seismic attenuation factor, Q, is constant throughout the stratigraphic interval. The source wavelet is injected as an impulsive pressure source from the top of the model, and the reflected wavefield is recorded by a co-incident receiver. The modelling is run for long enough to record a P-wave reflection from the deepest part of the model. To simulate acquisition and processing noise we add Gaussian noise equivalent to 2.5 % of the RMS amplitude of the modelled trace.

2.4. Monte Carlo ensemble analysis

We model multiple realisations by varying the random seed used to generate the background sedimentary noise. For each realisation we store the velocity and density model, the corresponding acoustic impedance pseudo-log and the modelled synthetic seismic trace. We estimate the spectral background of the acoustic impedance pseudo-log directly using LOWSPEC (Meyers, 2012). The spectral background of the synthetic seismic trace is estimated using the modified LOWSPEC approach (Section 2.2). Power spectrum estimation uses the multi-taper method (Thomson, 1982) implemented with the open-source Python library "multitaper" (Prieto, 2022). Prior to power spectrum estimation we isolate the stratigraphic interval by windowing and tapering (cosine tapers with half-width 5 % of the interval thickness), then de-mean and detrend the signal.

2.5. Eccentricity modulation and bundling analysis

An alternative technique to perform astrochronological testing is eccentricity-related amplitude modulation and bundling analysis (Zeeden et al., 2015). Here we demonstrate the borehole log and seismic application of TimeOpt (Meyers, 2015), an approach to invert for the optimal sedimentation rate for a stratigraphic series by simultaneously optimizing for eccentricity-related amplitude modulation (bundling) and the concentration of spectral power at the target frequencies. The result is an age domain stratigraphic series tuned to a predicted eccentricity model.

The modulator frequency is extracted by filtering to the carrier frequency band and taking the envelope using the Hilbert transform. Then a model of the eccentricity frequencies included in the modulator band is formed, with the amplitude and phase of each component frequency determined during the inversion. The Pearson's rank correlation coefficient can be used to quantify the match between the reconstructed model and the observed envelope of the carrier band. Simultaneously, the total spectral amplitude at the target frequencies is calculated. This procedure is repeated to obtain the correlation coefficients r^2_{env} and r^2_{pow} for the envelope and spectral amplitudes respectively, at each candidate sedimentation rate. The overall measure of goodness of fit, r^2_{opt}, is computed by multiplying the two together. The statistical significance of the result can be evaluated by comparing the best fitting r^2_{opt} of the analysed stratigraphic series to that of an ensemble of noise models that do not include an orbital signal. The TimeOpt concept can also be extended to invert for variable sedimentation rate models, from a simple linear change in sedimentation rate up to strongly discontinuous sedimentation models that include hiatuses and event beds (Meyers, 2015, 2019).

For typical TimeOpt applications the modulator frequencies would be the dominant eccentricity frequencies, and the carrier frequencies would be the dominant precession frequencies. Due to the relatively low resolution of the seismic data considered in this study, we expect to image little-to-none of the precession band, so instead we use the "long-period" 405 kyr eccentricity cycle as the modulator frequency and the "short-period" $\sim$ 125 and $\sim$ 93 kyr eccentricity cycles as the carrier frequencies. We cannot use simple AR(1) noise series to model the orbital signal free noise ensemble, as it would not properly model the limited bandwidth of seismic data (Section 2.1). Instead we apply an identical TimeOpt analysis to each of the realisations in the ensemble half with no added orbital signal generated during the Monte Carlo ensemble analysis (Section 2.4). For this study, we ignore variable sedimentation rate templates and simply invert for the mean sedimentation rate.

3. Simplified synthetic model

3.1. Model setup

The goal of the simplified synthetic model is to demonstrate seismic imaging of orbital cyclicity in a simplified example with common geological and geophysical parameters. The model consists of a 250 m interval with constant sedimentation rate of 15 cm ka^{-1} (i.e., 1.7 Ma–present) (Fig. 1). The background sedimentary noise is an AR(1) noise function with red noise parameter $\varphi = 0.75$, sampled every 5 cm (1 kyr). The orbital signal is an eccentricity-tilt series, constructed by taking the eccentricity and obliquity components of the Laskar et al. (2004) astronomical solution, sampled every 1 kyr and weighted to have roughly equal spectral power (Fig. 1e). For realisations with an added orbital signal, the sedimentary signal is a weighted sum of 25 % astronomical signal and 75 % background sedimentary noise. The P-wave velocity is

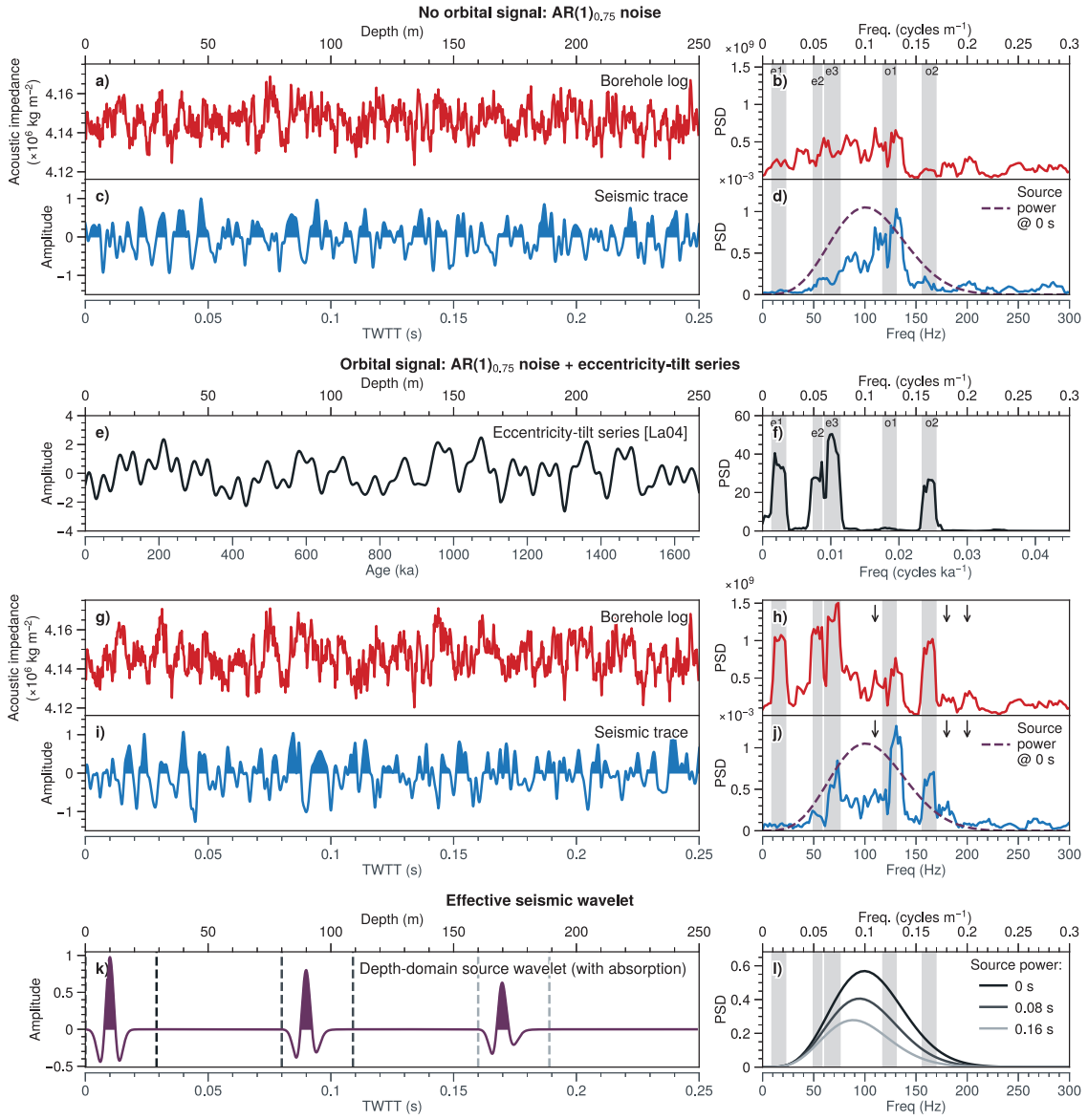

Fig. 1. Two realisations of the simplified synthetic model with sedimentary noise only (no orbital signal), and with sedimentary noise plus an orbital signal. (a) and (g) are the acoustic impedance pseudo-logs and (b) and (h) their respective power spectra. (c) and (i) are the seismic traces, and (d) and (j) their respective power spectra. Examples of spurious spectral peaks are marked with black arrows in (h) and (j). (e) is the eccentricity-tilt orbital signal and (f) the power spectrum (based on the astronomical solution from Laskar et al., 2004). (k) is the effective seismic wavelet at three different depths by stretching the injected source wavelet to depth domain and applying a forward-Q operator to simulate seismic absorption (Varela et al., 1993), and (l) the corresponding power spectra. Shaded zones represent the dominant eccentricity (e1 = 405 kyr, e2 = 125 kyr, e3 = 95 kyr) and obliquity (o1 = 56 kyr, o2 = 41 kyr) cycles for the interval 1.75 Ma–present. Power spectra are computed using the multi-taper method.

the sedimentary signal scaled to have a mean velocity of 2000 ms^{-1} and variance 200 ms^{-1}. The bulk density, ρ, is derived from the P-wave velocity, v_P, using Gardner's relation of $\rho = 0.31 v_P^{0.25}$ (Gardner et al., 1974). The seismic attenuation parameter is $Q = 80$ throughout the whole model.

The acoustic impedance pseudo-log and the seismic reflection response are modelled from the velocity and density series according to Section 2.3. The seismic source is a Ricker wavelet with dominant frequency 100 Hz (Fig. 1d,j). The seismic modelling is run for 8350 time-steps (0.76 s), and subsequently resampled to 1 ms. We model $n = 2000$ background sedimentary noise series, with and without an added orbital signal, resulting in an ensemble of $n = 4000$ total realisations.

3.2. Monte Carlo ensemble modelling results

The modelled acoustic impedance pseudo-logs are broadband, whereas the modelled seismic traces are narrowband, roughly corresponding to the bandwidth of the source wavelet, approximately 0.015–0.1 cycles m^{-1} (30–194 Hz; Fig. 1d,j). The effective seismic wavelet is represented by the source wavelet stretched to depth domain and filtered with a forward-Q attenuation and dispersion operator (Varela et al., 1993). Examples at three distinct travel times are presented in Fig. 1k and l, which can be compared to the modelled seismic traces (Fig. 1c and i). The power spectra of the modelled seismic traces are strongly frequency-dependent, with peak power around the dominant source frequency of 0.1 cycles m^{-1} (100 Hz). There is visible correlation of spectral peaks between the seismic and borehole log within the seismic bandwidth. To a first approximation, the seismic power

spectra appear similar to the borehole log filtered by the source wavelet. Outside the seismic bandwidth (<30 Hz and >194 Hz) the majority of the power is presumably due to the synthetic seismic noise (Section 2.3). For the realisation where no orbital signal is added (background sedimentary noise only) both the borehole and seismic power spectra show isolated, distinct (but spurious) peaks (Fig. 1d). For the realisation where an orbital signal is added the borehole log and seismic power spectra still show isolated and distinct peaks, however, many of the distinct peaks align with the dominant periodicity in the orbital signal (Fig. 1j). This indicates that the seismic trace has indeed imaged some of the orbital cyclicity (Fig. 1j). It should be noted that there are still several distinct spurious peaks that do not align with the orbital periodicities, these are false positives and should give us caution before conclusively interpreting any given distinct peak as representing orbital cyclicity.

Fig. 2 shows the spectral background estimation and significance levels for the same realisations as Fig. 1. For the acoustic impedance pseudo-log of the two realisations, the red noise parameter has been estimated as $\widehat{\varphi} = 0.72$ (no orbital signal) and $\widehat{\varphi} = 0.80$ (orbital signal), compared to the true model value of $\varphi = 0.75$. After whitening, both spectra appear roughly horizontal (Fig. 2a,b). Both realisations show several spectral peaks at >99 % confidence level, but the orbital signal realisation shows >99 % exceedances that align with e3 (95 kyr eccentricity), o1 and o2 (53 kyr and 41 kyr obliquity) (Fig. 2b,f). For the seismic case, the results appear more complex (Fig. 2c,d). Within the source bandwidth, the spectrum has been flattened compared to the raw spectrum, but is still sub-horizontal. For the realisation with an added orbital signal there is a >95 % exceedance at e3 (95 kyr eccentricity), o1 and o2 (53 and 41 kyr obliquity) (Fig. 2b,f).

The ensemble false positive rate for the borehole log is largely frequency-independent and approximates the inverse of the uncalibrated confidence level (i.e., a confidence level of 95 % gives, on average, a false detection rate of 5 % across all frequencies; Fig. 3a). This is consistent with findings in Meyers (2012) for directly sampled time series contaminated with AR(1) noise. For the seismic case, the false positive rate is broadly consistent with the uncalibrated confidence level within the seismic bandwidth (Fig. 3b). There is, however, a clear frequency-dependence, and the false positive rate is strongly inflated towards the edges of the seismic bandwidth where the source power is the lowest (and consequently the signal-to-noise is also lowest). The sensitivity plots show that for the borehole log, periodicities e1, e2, e3 (405 kyr, 125 kyr and 95 kyr eccentricity) and o1, o2 (56 kyr and 41 kyr obliquity) are detected, albeit with different true positive rates, presumably correlated to the respective spectral power from each orbital period in the astronomical solution (Fig. 3c). For the seismic case, the sensitivity is always lower than for the borehole log, with no or very little sensitivity shown for the e1 and e2 periods (405 kyr and 125 kyr eccentricity; Fig. 3d). For all cases, increasing the uncalibrated confidence level threshold from 90 % to 95 % to 99 % reduces the respective sensitivity. Receiver operating characteristic curves (often abbreviated as 'ROC curves') show the tradeoff between sensitivity (the average true positive rate) and specificity (the average true negative rate) as the confidence level is varied (Fig. 3e-i), where the 1:1 line represents the equivalent discriminatory power to a coin flip (i.e., random chance). Hypothesis testing for orbital cyclicity from the acoustic impedance log has clear discriminatory power (better than random chance) at periodicities e1, e2 and e3 (405 kyr, 125 kyr and 95 kyr eccentricity) and o2 (41 kyr obliquity). Hypothesis testing using the seismic, instead, has clear discriminatory power only at periodicities e3 (95 kyr eccentricity) and o2 (41 kyr obliquity). We note that periodicity e1 (405 kyr eccentricity) does not have a receiver operating characteristic curve for the seismic case simply because the frequency is so far outside the seismic bandwidth that there are no positive detections (true or false) in the ensemble (Fig. 3e). For all cases, both the sensitivity and specificity of the seismic case are lower than for the comparable borehole log case.

3.3. Short-period eccentricity modulation and bundling analysis

We perform short-period eccentricity TimeOpt analysis on the simplified synthetic ensemble to test for amplitude modulation and bundling (Section 2.5). The target periods are 405 kyr (modulator frequency), 125 kyr and 95 kyr eccentricity (carrier frequencies), and the data are filtered with a Taner filter with corner frequencies 0.007–0.0115 cycles ka^{-1} to extract the short-period eccentricity component. We test 200 sedimentation rates linearly spaced between 5 and 25 cm ka^{-1}.

We first apply the TimeOpt analysis to a single realisation (corresponding to Fig. 1) of the synthetic ensemble half that has an added astronomical signal, both to the borehole log (in depth domain) and to the equivalent modelled and whitened seismic trace (converted from TWTT to depth domain using the velocity model) (Fig. 4). The optimal sedimentation rate for both borehole log and seismic data (15.3 cm ka^{-1}) is very close to the true modelled sedimentation rate (15 cm ka^{-1}) (Fig. 4a and b). There is also well defined peak in the overall goodness of fit, r^2_{opt}, around the true sedimentation rate for both, although the peak goodness of fit for the seismic example is significantly lower than for the borehole log. The reconstructed long-period eccentricity models appear visually similar to the envelope of the short-period eccentricity band, and appear consistent between the borehole log and seismic cases (Fig. 4c and d). After conversion from depth to age domain with the best fitting sedimentation rate, spectral peaks align well with the target frequencies (Fig. 4i and j).

We repeat the TimeOpt analysis for every realisation in the ensemble half that does not have an added astronomical signal (noise ensemble). The distribution of the best fitting r^2_{opt} for the noise ensemble is shown in Figs. 4g and h, alongside the best fitting r^2_{opt} for the borehole log and seismic astronomical signal realisations, respectively. The borehole log goodness of fit is highly significant compared to the best fit r^2_{opt} of the noise ensemble (Fig. 4g). The seismic trace fit has relatively lower significance, but still higher than the majority of the noise ensemble (Fig. 4h), indicating that also the amplitude modulation and bundling analysis for the seismic case has high significance.

4. ODP Site 1084 (Cape Basin) real-world data example

4.1. Geological setting and data overview

ODP Site 1084 is located in the northern Cape Basin, offshore Namibia (Fig. 5), and was drilled as part of ODP Leg 175, whose main objective was to study sedimentary deposits related to the Benguela Current Upwelling System (Shipboard Scientific Party, 1998b). Drilling recovered 610 m of primarily organic-rich sediments, intermediate between hemipelagic mud and pelagic ooze, up to 4.62 Ma in age. The Cape Basin represents an ideal site to study the fine-scale influence of climate on sedimentation, and thus orbital cyclicity, due to its high sedimentation rates (~8 cm ka^{-1} in the early Pliocene to well above 15 cm ka^{-1} in the late Quaternary; Berger et al., 2002) resulting from the influence of the Benguela Current Upwelling System. At present day, this is one of the four major eastern boundary upwelling regions of the world ocean and is driven by the south-easterly trade winds, which result in zones of enhanced productivity. Studies along the southwest African continental margin have shown that the high productivity and upwelling initiation began at about 12–11.5 Ma, followed by an increase in mass accumulation rates of organic carbon and benthic foraminifera indicating an increase in productivity and coinciding with changes in the regional climate (Wefer et al., 2002; Diester-Haass et al., 2004). The resulting depositional structures were shaped by the interaction of climate, oceanic currents and sea level fluctuations, which modulated the physical properties of the marine sediments. In this way, P-wave velocity and density are affected, which are the parameters controlling acoustic impedance, and subsequently the seismic reflectivity. The

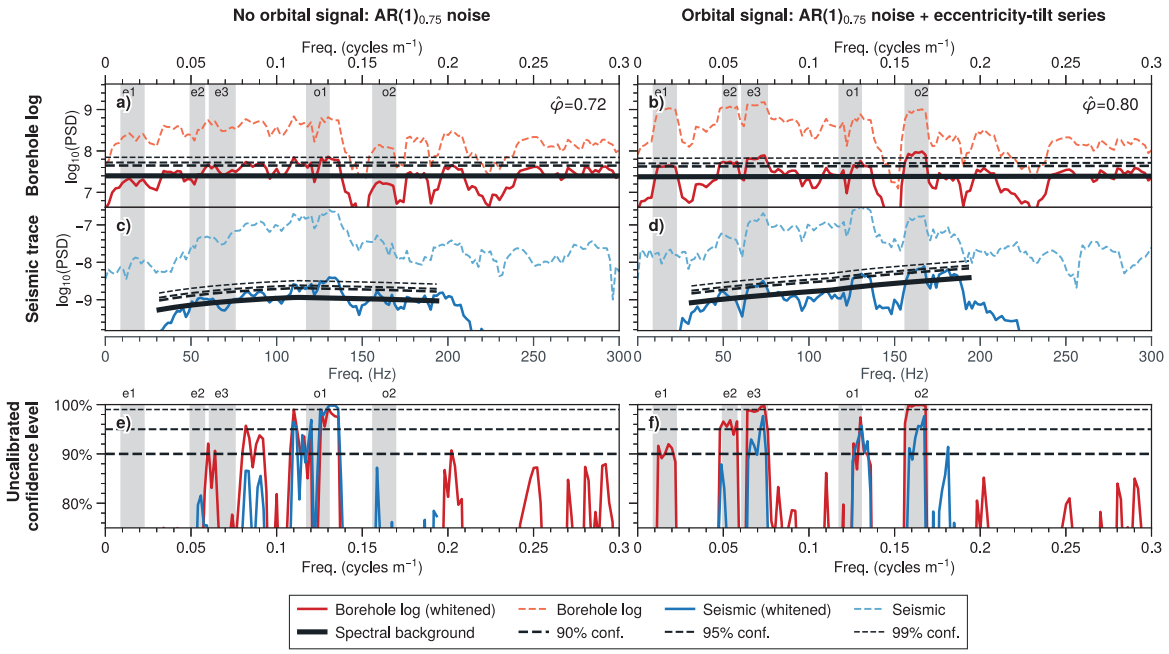

Fig. 2. Power spectra for two realisations of the simplified synthetic model with sedimentary noise only (no orbital signal), and with an added orbital signal (corresponding to Fig. 1). (a) and (b) are the acoustic impedance pseudo-logs, the raw spectra (dashed red) and the whitened spectra (solid red). (c) and (d) are the power spectra of the synthetic seismic traces, the raw (dashed blue) and the whitened spectra (solid blue). The estimated spectral baselines are plotted in solid black, and the parallel dashed black lines represent the corresponding confidence intervals. (e) and (f) are the confidence adjusted spectra, where the spectral baseline is at 0 %. Shaded zones represent the dominant eccentricity (e1 = 405 kyr, e2 = 125 kyr, e3 = 95 kyr) and obliquity (o1 = 56 kyr, o2 = 41 kyr) cycles for the interval 1.75 Ma–present. Power spectra are computed using the multi-taper method. (For interpretation of the references to colour in this figure legend, the reader is referred to the web version of this article.)

amplitudes of generated reflectors are higher with stronger and more abrupt changes in density or P-wave velocity of successive layers. Weigelt and Uenzelmann-Neben (2007) present examples of power spectra of seismic traces (and density logs) from several ODP Leg 175 sites in the Cape Basin which show distinct spectral peaks that mainly correspond to 100 kyr eccentricity cycles.

For this study we use the ODP Site 1084 age model from Berger et al. (2002) based on nannofossil and paleomagnetic data (Fig. 5d). The site was logged with a typical set of downhole logging tools, including the Hostile Environment Lithodensity Sonde (HLDS) and the Sonic Array Tool (SDT-LS) (ODP Hole 1084A; Wefer et al., 2002). Here we use the HDLS RHOM track as the bulk density log, and the processed SDT-LS VP1 track as the sonic velocity (Fig. 5b and c). ODP Site 1084 is intersected by seismic reflection profile AWI-96014, acquired as part of a site survey prior to drilling ODP Leg 175 (Fig. 5). The synthetic model aims to repeat the previous experiment (Section 3) with geological parameters that approximate the conditions at ODP Site 1084 and geophysical parameters that approximate seismic reflection profile AWI-96014.

We estimate the seismic wavelet by shift-stacking the seafloor reflection on seismic profile AWI-96014 (Blondel et al., 2023). This method assumes that the seismic profile approximates a zero-offset image, and that the seafloor represents an isolated positive impedance contrast. Over the length of the profile the sub-seafloor geology varies, meaning that after shift-stacking the seafloor reflections constructively interfere, whereas the sub-seafloor reflections are cancelled out. The result is a wavelet that approximates the far-field seismic source wavelet (Fig. 5e). The dominant frequency of the estimated seismic wavelet is approximately 80 Hz.

We perform a borehole-seismic correlation by interactively picking a time-depth model in OpendTect seismic interpretation software[1] using several control points, which are used to convert both the sonic velocity and density logs to TWTT. The product of the two logs gives the acoustic impedance and the corresponding reflectivity series (Fig. 5h). We convolve the reflectivity series with the estimated seismic wavelet to produce a synthetic seismic trace at the borehole location (Fig. 5j). This is visually correlated with the 5 closest traces to the borehole in AWI-96014 (Fig. 5i). The control points are linearly interpolated to give a time-depth model for ODP Site 1084 (Fig. 5g). We convert from TWTT to stratigraphic age domain by first interpolating from TWTT to depth using the time-depth model, then interpolate to age domain using the depth-age model (Fig. 5d).

4.2. ODP Site 1084 borehole and seismic cyclostratigraphy

Fig. 6 shows the ODP Site 1084 acoustic impedance pseudo-log and the closest seismic trace from seismic profile AWI-96014 stretched from TWTT to age domain, alongside their respective power spectra. The borehole log power spectrum shows distinct spectral peaks that correlate with, or fall close to, the orbital periods for e1, e2, e3 (400 kyr, 125 kyr and 95 kyr eccentricity), o1 (56 kyr obliquity) and p1 and p2 (24 kyr, 22 kyr precession) (Fig. 6b). The seismic trace power spectrum, instead, shows a clear distinct spectral peak only at e3 (95 kyr eccentricity) (Fig. 6d).

Figs. 6g-h show the borehole log and seismic trace spectra after spectral whitening and spectral baseline estimation. The confidence-adjusted borehole log spectrum shows spectral peaks at >90 % confidence level for orbital periods e1, e2 (400 kyr and 125 kyr eccentricity), o2 (41 kyr obliquity) and p2 (22 kyr precession), and at >95 % confidence level for e3 (95 kyr eccentricity) and p1 (24 kyr precession). There is also a >95 % confidence level peak just outside the bounds for orbital period o1 (56 kyr obliquity). If this is not a spurious peak, this misalignment could be caused by errors in the depth-age model. There is clear evidence of several spurious >90 % confidence level spectral peaks that are not associated with the dominant orbital periods. The confidence-adjusted seismic trace spectrum shows spectral peaks at

[1] https://dgbes.com/software/opendtect

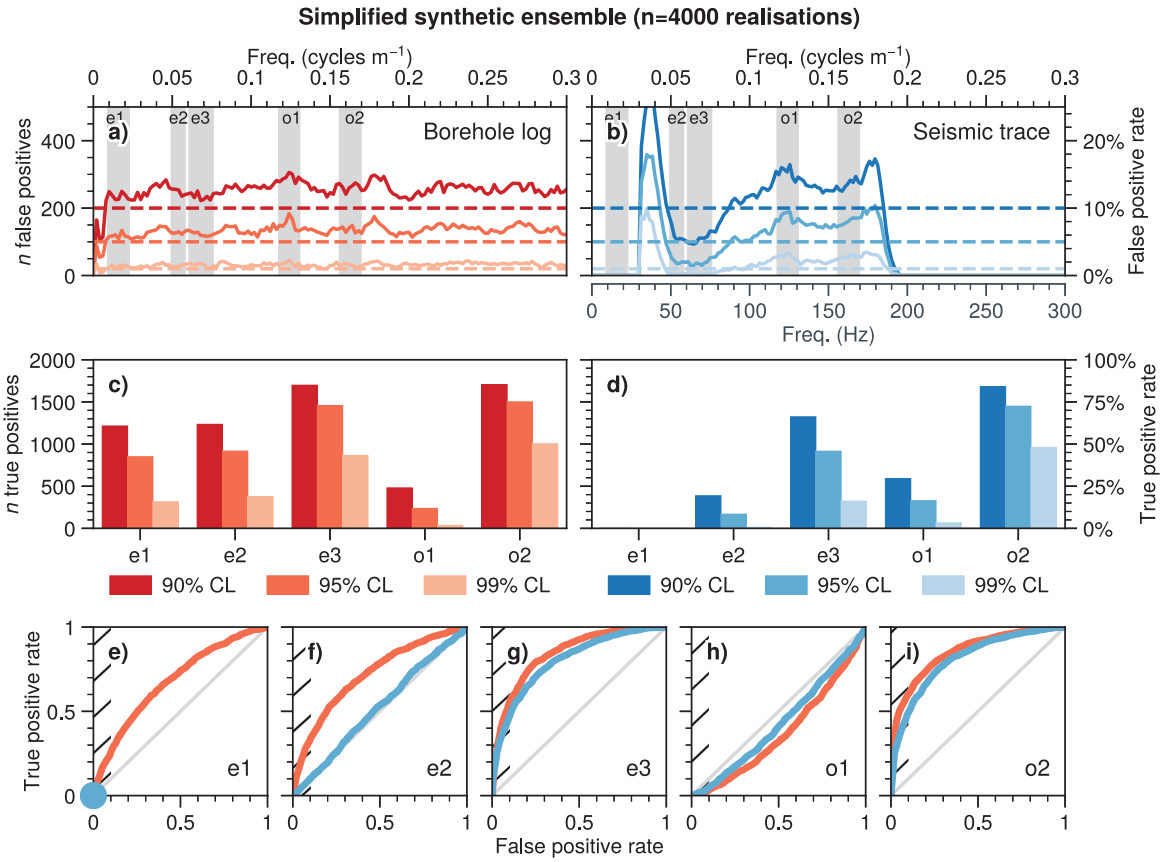

Fig. 3. Simplified synthetic model false positive rates at each spectral frequency, relative to the 90 %, 95 % and 99 % confidence levels for (a) the borehole log and (b) the seismic case (note that the frequency axes cover different ranges). (c) and (d) are the true positive rates for the dominant eccentricity (e1 = 405 kyr, e2 = 125 kyr, e3 = 95 kyr) and obliquity (o1 = 56 kyr, o2 = 41 kyr) cycles. (e-i) Receiver operating characteristic curves for each orbital term, showing the discriminatory power as the confidence level is varied (grey lines indicate 1:1 correspondence, i.e., equivalent to a coin flip).

>90 % confidence level for orbital periods e2, e3 (125 kyr and 95 kyr eccentricity) and o2 (41 kyr obliquity), and at >99 % confidence level for o1 (56 kyr obliquity). There is clear evidence of several spurious >90 % confidence level spectral peaks that are not associated with the dominant orbital periods, including one at >99 % confidence level between the eccentricity and obliquity bands. The >99 % confidence level spectral peaks close to p3 (19 kyr precession) are clearly spurious, as they fall well outside the seismic bandwidth, and likely represent artifical over-boosting of noise at the edges of the source bandwidth during spectral whitening.

The statistically significant detections are consistent with previous observations of distinct spectral peaks aligned with 400 kyr and 100 kyr eccentricity cyles and 41 kyr obliquity cycles from both borehole log (density log) and seismic traces at other sites drilled in the Cape Basin during ODP Leg 175 (Weigelt and Uenzelmann-Neben, 2007).

4.3. Model setup

The role of our ODP Site 1084 synthetic model is to demonstrate the application of seismic cyclostratigraphy in a scenario with real-world geological and geophysical parameters: variable sedimentation rate, a variable velocity model and a non-parametric source wavelet (Fig. 5). The ODP Site 1084 synthetic model consists of a water layer above a 550 m stratigraphic interval starting from the seafloor, with a sedimentation rate that varies between 7 and 22 cm ka^{-1} (from 4.2 Ma–present; Fig. 5d). The background sedimentary noise is AR(1) noise with red noise parameter $\varphi = 0.9$, chosen to approximately fit the observed power from the ODP Site 1084 acoustic impedance pseudo-log, sampled every 5 cm (approx. 1 kyr at the seafloor). The orbital signal is an eccentricity-tilt-precession series, constructed by taking the eccentricity, obliquity and precessional components of the Laskar et al. (2004) astronomical solution, sampled every 1 kyr and weighted to have roughly equal spectral power (Fig. 7e). For realisations with an added orbital signal, the sedimentary signal is a weighted sum of 25 % astronomical signal and 75 % background sedimentary noise. The P-wave velocity and bulk density models use the background trend from Fig. 5b and c, respectively, smoothed with a 400 m Gaussian smoother, and adding the sedimentary signal scaled to have a standard deviation of 50 ms^{-1} and 70 g cm^{-3} respectively (chosen to approximately match the ODP Site 1084 borehole logs). The attenuation parameter is $Q = 120$ within the stratigraphic interval.

The acoustic impedance pseudo-log and the seismic reflection response are modelled from the velocity and density series (Section 2.3; Fig. 7a-d,g-j). The seismic source is the estimated seismic wavelet from profile AWI-96014 (Section 4.1; Fig. 5f). The seismic modelling is run for 24 800 timesteps (2.48 s), and subsequently resampled to 1 ms. We model $n = 1000$ background sedimentary noise series, with and without an added orbital signal, resulting in an ensemble of $n = 2000$ total realisations.

4.4. Monte Carlo ensemble modelling results

For the individual realisations there is visible correlation of spectral peaks between the seismic and borehole log within the seismic bandwidth (Fig. 7), albeit less clearly than for the simplified synthetic model (Fig. 1), due to the more complicated frequency response of the estimated source wavelet. For the realisation where no orbital signal is added (background sedimentary noise only) both the borehole and

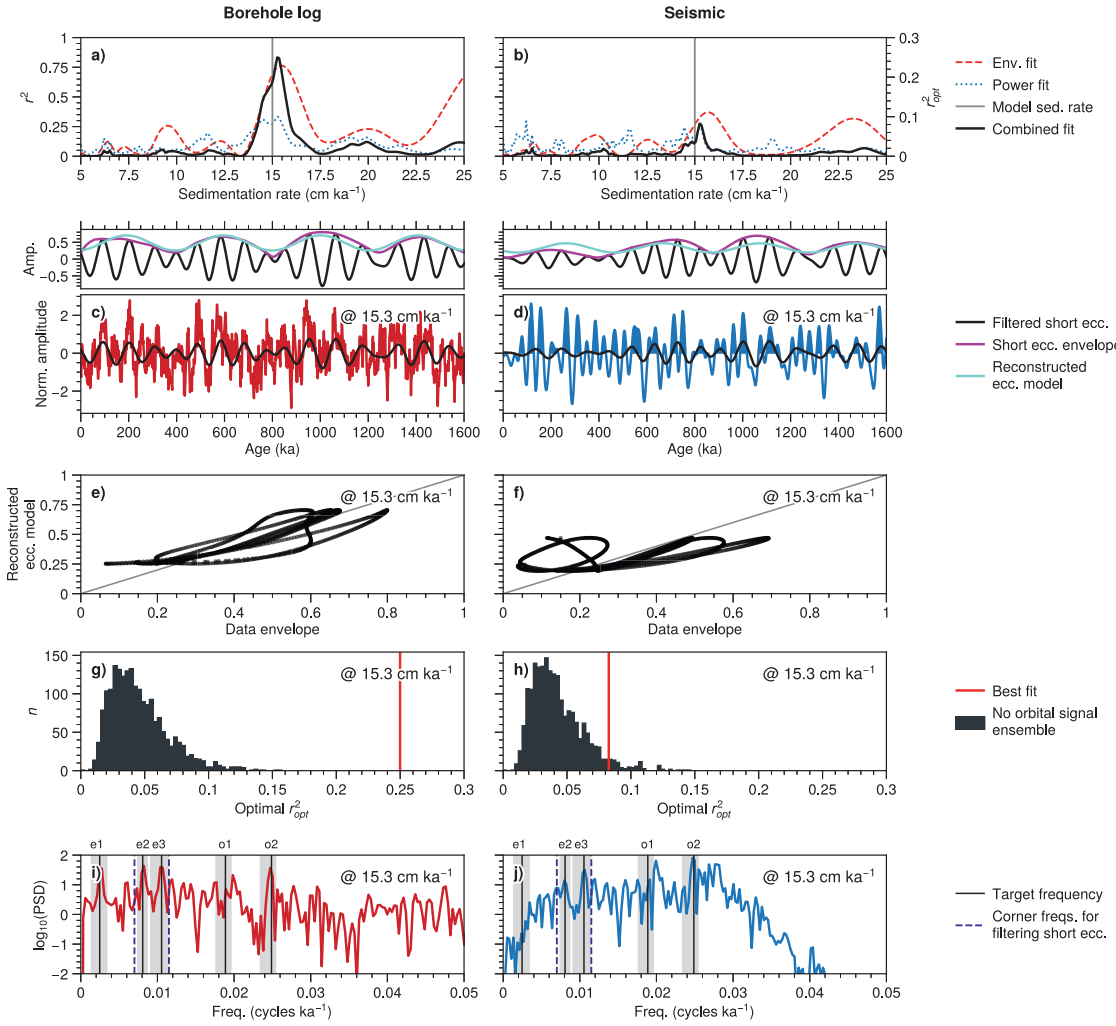

Fig. 4. Short-period eccentricity modulation and bundling analysis (TimeOpt) for both the borehole log and whitened seismic trace for one realisation of the simplified synthetic model that includes an orbital signal (Figs. 1g, i). (a-b) Goodness-of-fit criteria for each candidate sedimentation rate. (c-d) Data scaled and stretched to age domain with the best fitting sedimentation rates, with comparison (above) between the envelope of the short-period eccentricity band and the reconstructed eccentricity model. (e-f) Crossplot of the fit between the data amplitude envelope and the reconstructed eccentricity model. (g-h) The optimal r^2_{opt} for this realisation compared to a histogram of r^2_{opt} values for the ensemble of simplified synthetic models that do not include an orbital signal. (i-j) Power spectra of the data in age domain with the dominant orbital periods shaded, and the TimeOpt target eccentricities and short-period eccentricity band indicated (blue dashed lines). Shaded zones represent the dominant eccentricity (e1 = 405 kyr, e2 = 125 kyr, e3 = 95 kyr) and obliquity (o1 = 56 kyr, o2 = 41 kyr) cycles for the interval 1.75 Ma–present. (For interpretation of the references to colour in this figure legend, the reader is referred to the web version of this article.)

seismic power spectra show isolated, distinct (but spurious) peaks (Fig. 7b,d). For the realisation where an orbital signal is added the borehole and seismic power spectra still show isolated and distinct peaks, however many of the distinct peaks align with the dominant periodicity in the orbital signal. This indicates that the seismic trace has imaged some of the orbital cyclicity.

Both realisations (see also the spectral background estimation and significance levels in Fig. 8) show several spectral peaks in the borehole log at >99 % confidence level, but the orbital signal realisation shows >99 % exceedances that align with e1 and e3 (405 kyr and 95 kyr eccentricity) and o2 (41 kyr obliquity) (Fig. 8f). For the seismic case, the results appear more complex. The whitening procedure has artificially boosted the spectral power at the edges and outside the source bandwidth. Within the source bandwidth, the spectrum has been flattened compared to the raw spectrum and is roughly horizontal (Fig. 8c,d). Both realisations show several spectral peaks exceeding the >99 % confidence level, and for the realisation with an added orbital signal there is a >99 % exceedance at e2 and e3 (125 kyr and 95 kyr eccentricity) and o2 (41 kyr obliquity), and a >95 % exceedance at p1 (24 kyr precession).

For the Monte Carlo ensemble modelling the false detection rate for the borehole log is largely frequency-independent and approximates the inverse of the uncalibrated confidence level (i.e., a confidence level of 95 % gives, on average, a false detection rate of 5 % across all frequencies) (Fig. 9a). For the seismic case, the false detection rate is higher than the uncalibrated confidence level within the seismic bandwidth and there is a very strong frequency-dependence (Fig. 9b). The sensitivity plots show that for the borehole log at confidence level 90 % only e2, e3 (125 kyr and 95 kyr eccentricity), o2 (41 kyr obliquity) and p1, p2 and p3 (24 kyr, 22 kyr and 19 kyr precession) are correctly detected at a rate of >75 % (Fig. 9c). For the seismic case the sensitivity is always lower than for the borehole log, with almost zero sensitivity shown for the e1 (405 kyr eccentricity) period and significantly lower sensitivity show for the precession periods (Fig. 9d). For all cases, increasing the uncalibrated confidence level threshold from 90 % to 95 % to 99 % reduces the sensitivity, as expected. Receiver operating characteristic curves show the tradeoff between sensitivity (the average true positive rate) and specificity (the average true negative rate) as the confidence

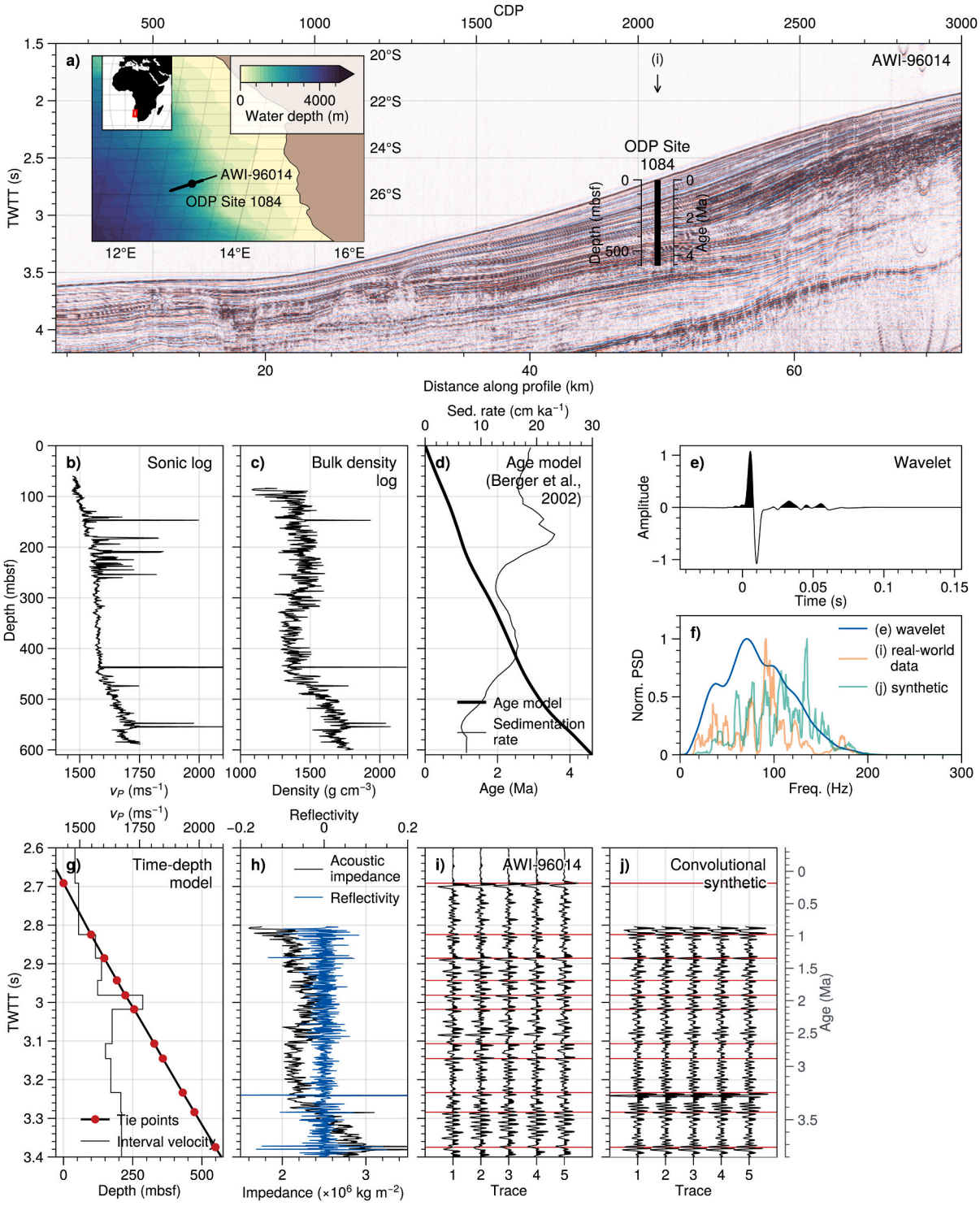

Fig. 5. (a) Seismic reflection profile with location of ODP Site 1084 and age-depth overlay. (b) Sonic and (c) bulk density borehole logs (note that these logs start below the seafloor due to the hole casing). (d) Age-depth model (thick line) and corresponding sedimentation rate (thin line). (e) Estimated seismic wavelet and (f) power spectrum, with power spectra of (i) and (j) for comparison. (g) Time-depth model (thick line) and corresponding interval velocity (thin line) after seismic-log correlation. (h) Acoustic impedance (black) and reflectivity (blue) in TWTT. (i) Seismic traces adjacent to the borehole (location in (a)) and (j) the corresponding convolutional synthetic traces, used to validate the time-depth model. TWTT: two-way traveltime. (For interpretation of the references to colour in this figure legend, the reader is referred to the web version of this article.)

level is varied (Fig. 9e-l). Hypothesis testing for orbital cyclicity from the acoustic impedance pseudo-log has clear resolving power (better than random chance) at periodicities e1, e2 and e3 (405 kyr, 125 kyr and 95 kyr eccentricity), o2 (41 kyr obliquity) and p1, p2 and p3 (24 kyr, 22 kyr and 19 kyr precession). Hypothesis testing using the seismic trace, instead, has clear resolving power only at periodicities e3 (95 kyr eccentricity), o2 (41 kyr obliquity) and p1 (24 kyr precession). For all cases both the sensitivity and specificity of the seismic case are lower than for the comparable borehole log case.

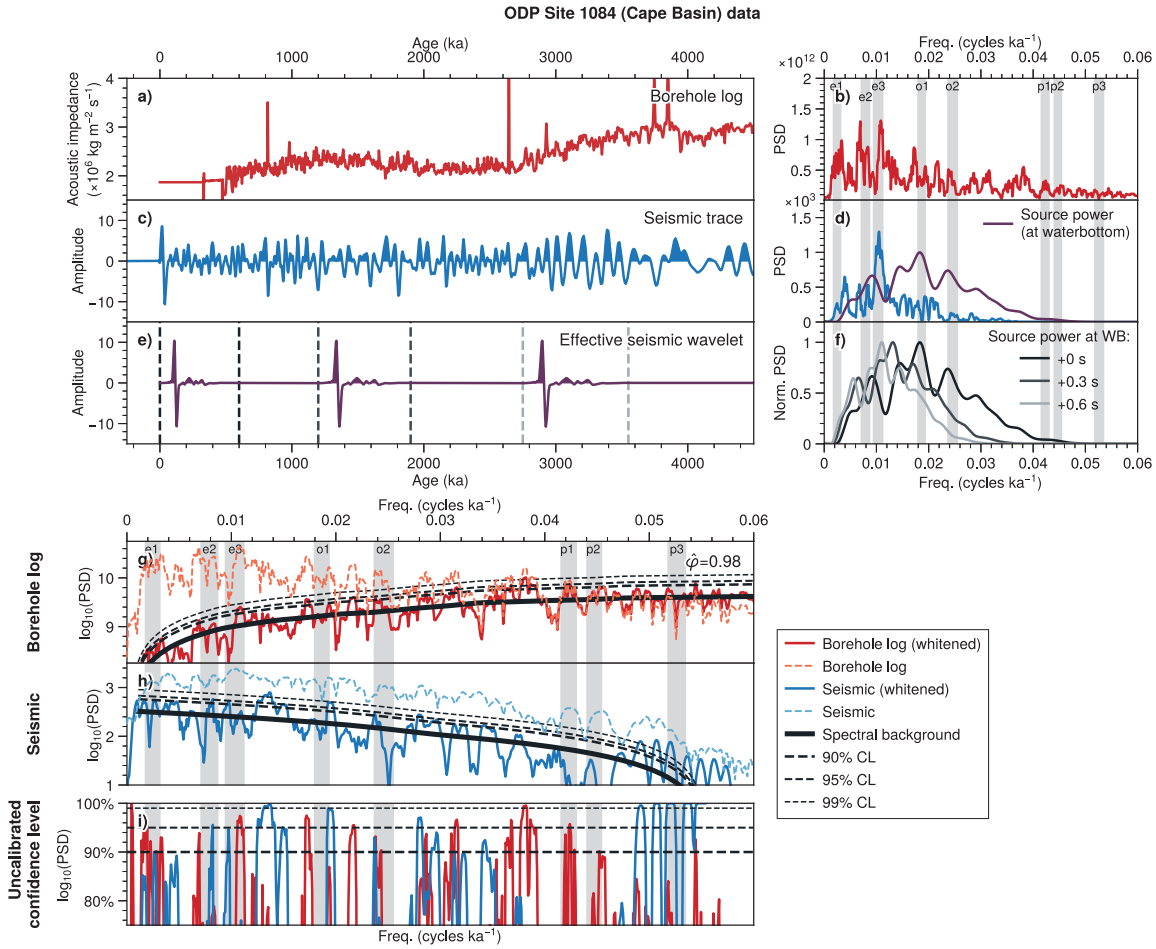

Fig. 6. ODP Site 1084 (Cape Basin) real-world data. (a) The acoustic impedance pseudo-log stretched to age domain using the age-depth model (Fig. 4d), and (b) the corresponding power spectrum. Values younger than approximately 250 ka are extrapolated due to the hole casing. (c) The corresponding recorded seismic trace, stretched to age domain, and corresponding power spectrum (d). (e) The effective seismic wavelet at three different ages by stretching the estimated seismic wavelet to age domain and (f) the corresponding power spectra. (g) The raw (dashed) and whitened (solid) power spectra for the borehole log. (h) The raw (dashed) and whitened (solid) seismic trace power spectra. (i) Both the borehole log and seismic confidence adjusted spectra, where the spectral baseline is at 0 %. Shaded zones represent the dominant eccentricity (e1 = 405 kyr, e2 = 125 kyr, e3 = 95 kyr), obliquity (o1 = 56 kyr, o2 = 41 kyr) and precession (p1 = 24 kyr, p2 = 22 kyr, p3 = 19 kyr) cycles for the interval 4.6 Ma–present. Power spectra are computed using the multi-taper method.

4.5. Short-period eccentricity modulation and bundling analysis

We perform short-period eccentricity TimeOpt analysis on both the ODP Site 1084 real-world data (Fig. 5) and the ODP Site 1084 synthetic model (Fig. 7) to test for amplitude modulation and bundling (Section 2.5). The target periods and filter parameters to extract the short-period eccentricity component are the same as for the simplified synthetic model (Section 3.3). We test 100 sedimentation rates linearly spaced between 10 and 20 cm ka^{-1}. The ODP Site 1084 realistic sedimentation rate model is strongly variable, from approximately 7–22 cm ka^{-1}, with a mean sedimentation rate of 14.8 cm ka^{-1} (Berger et al., 2002, Fig. 5d). For this demonstration we simply invert for the mean (constant) sedimentation rate.

We first apply the TimeOpt analysis to both the ODP Site 1084 real-world data (Fig. 5), both to the borehole log (depth domain) and to the equivalent whitened seismic trace (converted from TWTT to depth domain using the velocity model) (Figs. 10a,b). The optimal sedimentation rate for the borehole log (14.6 cm ka^{-1}) is very close to the mean model sedimentation rate (14.8 cm ka^{-1}) (Fig. 10a). The reconstructed long-period eccentricity models appear visually similar to the envelope of the short-period eccentricity band (Fig. 10e). After conversion from depth to age domain with the best fitting sedimentation rate, spectral peaks align well with the target frequencies (Fig. 10q). For the seismic trace, the optimization is less successful, yielding an optimal sedimentation rate of 12.8 cm ka^{-1} (Fig. 10b). The reconstructed long-period eccentricity models do not correlate well with the envelope of the short-period eccentricity band (Fig. 10f), and the age domain spectral peaks do not appear to align well with the target frequencies (Fig. 10r).

We then apply the TimeOpt analysis to a single realisation of the synthetic ensemble half that has an added astronomical signal (corresponding to Fig. 7). The optimal sedimentation rate for the borehole log (15.5 cm ka^{-1}) is close to the true mean model sedimentation rate (14.8 cm ka^{-1}), with a well defined peak in the overall goodness of fit, r^2_{opt}, around the mean model rate (Fig. 10c). The reconstructed long-period eccentricity models appear visually similar to the envelope of the short-period eccentricity band (Fig. 10g). After conversion from depth to age domain with the best fitting sedimentation rate, spectral peaks align well with the target frequencies (Fig. 10s). For the seismic trace, the optimization is less clear, yielding a goodness of fit with a large spread around the mean model sedimentation rate, and a peak fit at 16.3 cm ka^{-1} (Fig. 10d).

We repeat the TimeOpt analysis for every realisation in the ensemble half that does not have an added astronomical signal (noise ensemble). The distribution of the best fitting r^2_{opt} for the noise ensemble is shown in Figs. 10m and o (borehole log) and Figs. 10n and p (seismic trace), alongside the best fitting r^2_{opt} for both the ODP Site 1084 real-world data

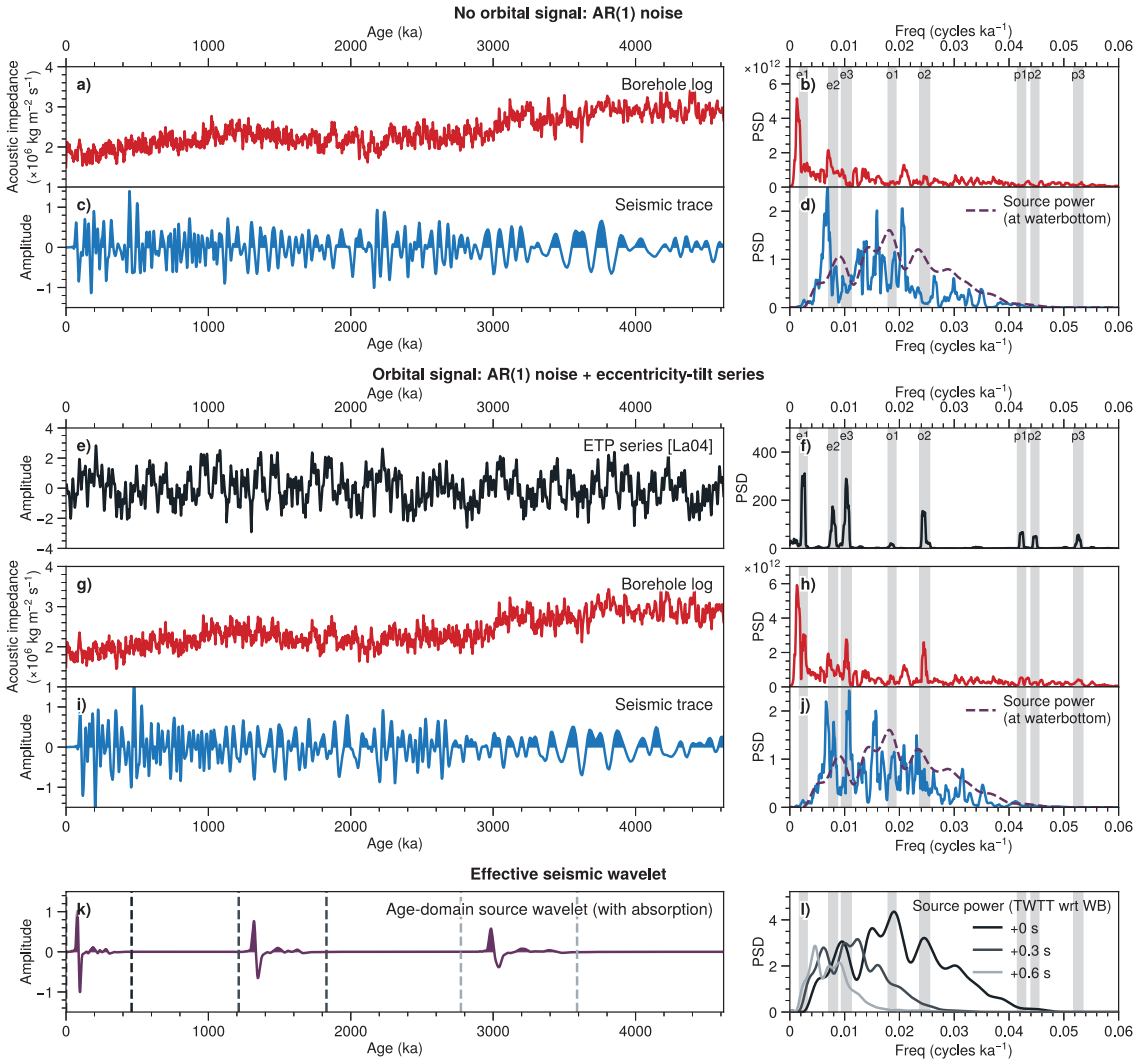

Fig. 7. Two realisations of the ODP Site 1084 (Cape Basin) synthetic model with sedimentary noise only (no orbital signal), and with an added orbital signal. (a) and (g) are the acoustic impedance pseudo-logs and (b) and (h) their respective power spectra. (c) and (i) are the modelled seismic reflection traces, and (d) and (j) their respective power spectra. (e) is the eccentricity-tilt-precession (ETP) orbital signal (based on the astronomical solution from Laskar et al., 2004) and (f) the power spectrum. (k) is the effective seismic wavelet at three different ages by applying a forward-*Q* operator to simulate seismic absorption (Varela et al., 1993) to the injected source wavelet and stretching to age domain, and (l) the corresponding power spectra. Shaded zones represent the dominant eccentricity (e1 = 405 kyr, e2 = 125 kyr, e3 = 95 kyr), obliquity (o1 = 56 kyr, o2 = 41 kyr) and precession (p1 = 24 kyr, p2 = 22 kyr, p3 = 19 kyr) cycles for the interval 4.6 Ma–present. Power spectra are computed using the multi-taper method.

and synthetic cases. The relative significance is much lower than for the simplified synthetic model ensemble (Fig. 4), likely due to the variable sedimentation rate in the model. It should be noted that the goodness of fit for the real-world data cases (Figs. 10m,n) is not directly comparable to the (synthetic) noise ensemble, due to the difference in signal-to-noise ratio and the presence of the very high amplitude reflections from diagenetically altered thin layers which are not included in the synthetic model (Weigelt and Uenzelmann-Neben, 2007).

5. Discussion

5.1. *Preservation of orbital signals in acoustic impedance*

Traditional cyclostratigraphic methods largely rely on directly sampled geochemical, biostratigraphic and physical parameters, or calculated indices, magnetic susceptibility, and colour reflectance. Not all the parameters commonly used to identify orbital cyclicity in sedimentary sequences are, considered alone, paleoenvironmental proxies. Their relevance to paleoenvironment and paleoclimate emerges from a combined, multi-proxy analysis (e.g., Berger, 2012; Hepp et al., 2006). For seismic reflection images to encode information on orbital forcing, the signal of orbitally-forced climate variation first must be preserved in the acoustic impedance (the product of the seismic velocity and density of the sediments).

Following an Earth Systems Filter model (e.g., Meyers, 2019), cyclical variations in the Earth's orbital parameters (eccentricity, obliquity and precession) induce variation in the average insolation at a given latitude (the astronomical signal) which perturbs the climate system. Due to internal feedback and noise in the climate system this climate signal is a noisy, filtered version of the original orbital signal. These climate changes influence the sedimentary and depositional systems and may thus be reflected in the stratigraphic record. This record is again noisy due to incomplete preservation and exposure, and further disturbed by syn- and post-depositional noise (e.g., bioturbation, deformation and diagenesis) (Hilgen et al., 2015). The stratigraphic record is subject to compaction during burial, which alters the orbital signal both on a local scale (e.g., differential compaction between lithologies) and a global scale (i.e., older sediments are more compacted

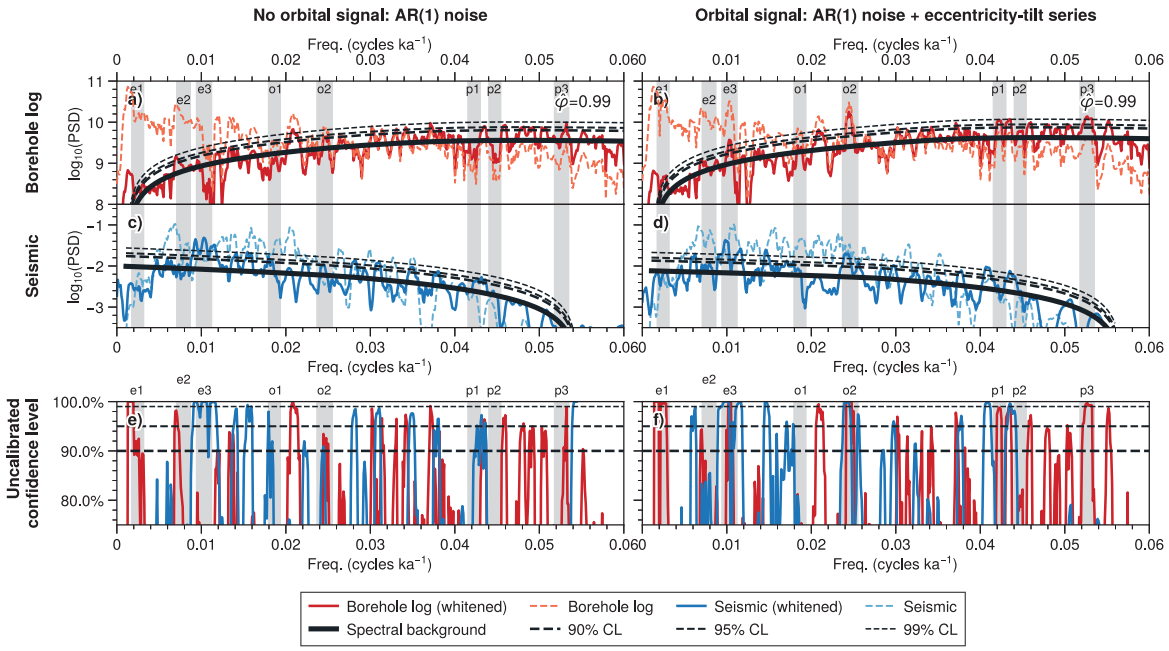

Fig. 8. Power spectra for two realisations of the ODP Site 1084 (Cape Basin) synthetic model with sedimentary noise only (no orbital signal), and with an added orbital signal (corresponding to Fig. 7). (a) and (b) are the acoustic impedance pseudo-log, the raw spectrum (dashed red) and the whitened spectrum (solid red). (c) and (d) are the power spectra of the synthetic seismic traces, the raw (dashed blue) and the whitened spectra (solid blue). The estimated spectral baselines are plotted in solid black, and the parallel dashed black lines represent the corresponding confidence intervals. (e) and (f) are the confidence adjusted plots, where the spectral baseline is at 0 %. Shaded zones represent the dominant eccentricity (e1 = 405 kyr, e2 = 125 kyr, e3 = 95 kyr), obliquity (o1 = 56 kyr, o2 = 41 kyr) and precession (p1 = 24 kyr, p2 = 22 kyr, p3 = 19 kyr) cycles for the interval 4.6 Ma–present. Power spectra are computed using the multi-taper method. (For interpretation of the references to colour in this figure legend, the reader is referred to the web version of this article.)

with depth due to lithostatic loading). The systematic stratigraphic distortion with depth caused by loading can be reversed assuming an accurate age model is available. Compaction in general, however, will act to reduce porosity which will reduce the relative difference in velocity and density between beds and thus reduce the magnitude of impedance contrasts. This will reduce the amplitude of any preserved orbital signals above the noise floor. Finally, the seismic reflection experiment that images the stratigraphic interval has its own inherent filtering and distortion effects (Section 2.1). Any orbital signal that is preserved in the acoustic impedance at the time of deposition will likely be strongly distorted and contaminated with large amounts of noise by the time it is imaged by a geophysical reflection experiment.

The seismic velocity and bulk density of fully-saturated marine sediments are strongly correlated with the sediment composition (lithology) and the porosity, which is in turn strongly coupled to the sediment texture and grain size distribution (Castagna et al., 1985; Gardner et al., 1974; Mavko et al., 2009). As such, plausible common mechanisms that might preserve climate signals in the acoustic impedance could include the clay content, the degree of sorting, diagenesis, sedimentation rate and post-deposition burial and differential compaction. Clay content may vary strongly with paleo-sea level, which depends on climate through glacial-interglacial cycles. In deep-water systems, the degree of sorting can be coupled to paleocurrent speed, which can be coupled to climatic variations. Biogenic silica in sediment drifts on glacial margins represents a proxy for sea ice extent and paleoproductivity (Hillenbrand and Fütterer, 2002). Before diagenesis, the accumulation of biogenic silica in marine sedimentary sequences induces compaction disequilibrium and petrophysical changes that meaningfully affect reflectivity (e.g., Volpi et al., 2003). Sedimentation rate also has a strong impact on the degree of sorting and can induce post-burial differential compaction and thus generate astronomically-forced density variation. Fluctuations in terrigenous delivery to the continental rise has been associated with variation in size of the ice sheets (Grützner et al., 2003).

In sedimentary systems where the sorting is strongly modulated by bottom current speed, e.g., contourites, a large proportion of the reflectivity (typically relatively high amplitude horizons in seismic data) is also modulated by climate signals. Cyclic deposition related to variation in bottom current velocity is suggested to be driven by orbital forcing (Stow et al., 1998) and has been identified in the seismic reflection characteristics of both sparker and airgun multi-channel seismic data (Stow et al., 2002). Seismic cyclicity in contourites is generally described as an alternation of two reflection patterns: relatively transparent (attributed to homogeneous mud deposited by slow currents), and relatively high amplitude (attributed to silt or sand deposited by faster currents). This cyclicity is considered to represent repeated sequences of grain size variation at various (orbital) scales. Many studies describe this contouritic seismic cyclicity (e.g., Llave et al., 2001, 2020; Vandorpe et al., 2011; Liu et al., 2020), although most do not include a proper spectral analysis, instead inferring the presence of an orbital control by counting the number of visually distinct seismic units within a known time interval. A well-developed cyclostratigraphic pattern has been identified in the Gulf of Cadiz contourite depositional system with spectral analyses on normalized gamma ray logs time-series (Hernández-Molina et al., 2016), showing orbital cyclicity in the range of the Milanković temporal cycles (22 kyr, 23 kyr and 24.5 kyr precession, 44 kyr and 55 kyr obliquity and 85 kyr, 96 kyr, and 105 kyr short-term eccentricity) and periods of 406 kyr and 420 kyr correlated with long-term eccentricity cycles. In addition, peaks around 2 Ma were tentatively correlated with the eccentricity term around 2.4 Ma (related to Earth–Mars secular resonance), and those around 800 ka to a double mode (two times the period) of the ~400 ka long-term eccentricity or to a possible non-linear combination of other periods. Sedimentary cycles at around 800 and 400 ka are visually observed in the multi-channel seismic data crossing IODP Expedition 339 sites (Hernández-Molina et al., 2016).

Post-deposition mineral transformation may, however, affect the seismic velocity and bulk density of sediments independently from

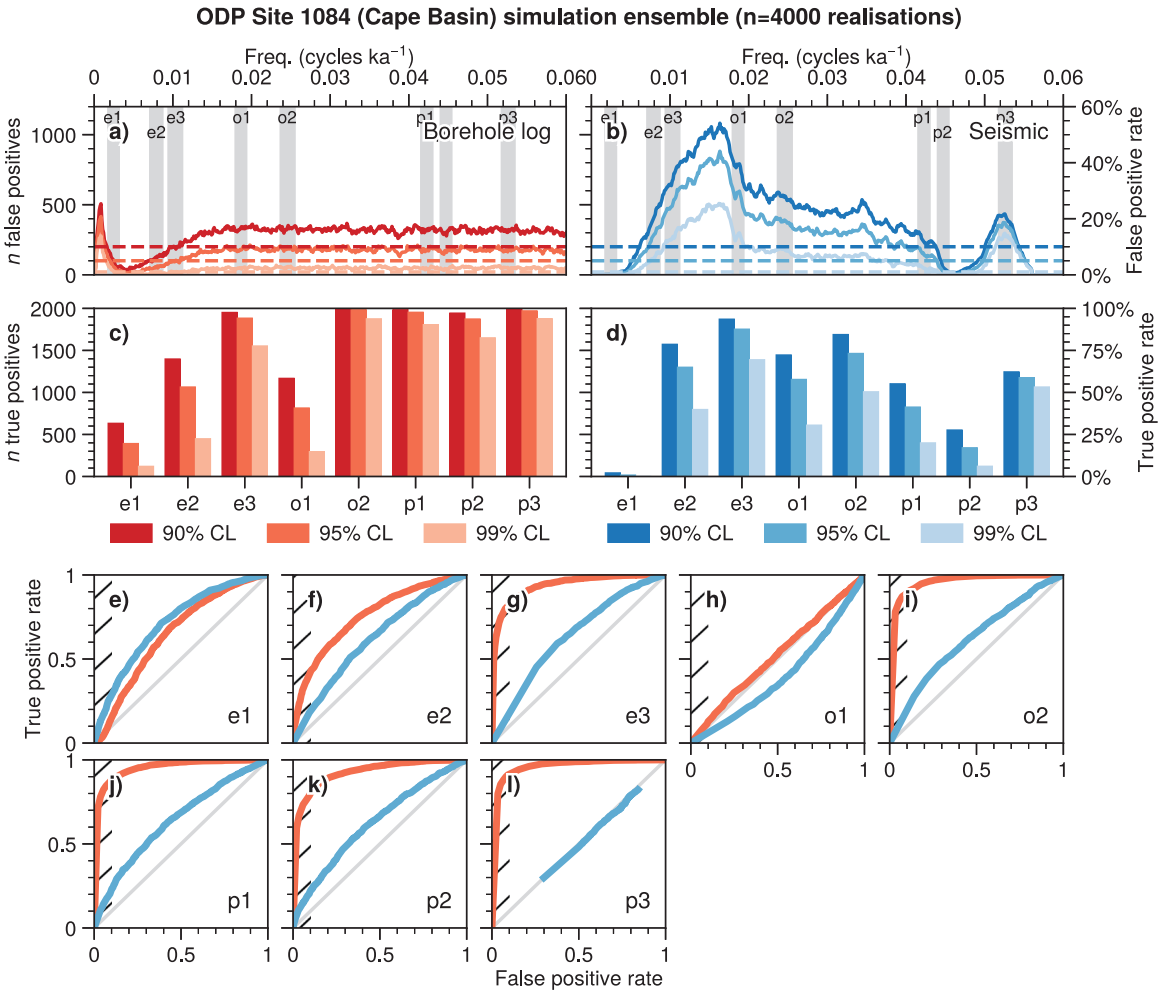

Fig. 9. ODP Site 1084 (Cape Basin) synthetic model false positive rates at each spectral frequency, relative to the 90 %, 95 % and 99 % confidence levels for (a) the borehole log and (b) the seismic case. (c) and (d) are the distributions of the true positive rate for the dominant eccentricity (e1 = 405 kyr, e2 = 125 kyr, e3 = 95 kyr), obliquity (o1 = 56 kyr, o2 = 41 kyr) and precession (p1 = 24 kyr, p2 = 22 kyr, p3 = 19 kyr) periodicities. (e-l) Receiver operating characteristic curves for each orbital term, showing the discriminatory power as the confidence level is varied (grey lines indicate the 1:1 correspondence, i.e., equivalent to a coin flip).

changes in climate. Clay mineral transformation (illite to smectite, e.g., Pytte and Reynolds, 1989), opal-A to -CT transformation (e.g., Volpi et al., 2003), and mineral dehydration such as illite dehydration (Hall et al., 1986) and gypsum dehydration to anhydrite (Jowett et al., 1993) induce meaningful bulk density changes and fluid release that strongly affect acoustic impedance and reflectivity. Carbonate diagenesis can also induce meaningful porosity changes (e.g., Moore, 1989). All the aforementioned post-depositional transformations have the potential to induce additional noise in the climatically-modulated acoustic impedance.

The potential of physical properties to preserve the signal of orbital cyclicities is already widely recognized. Common parameters used to perform conventional cyclostratigraphic analysis are bulk density (e.g., Zeeden et al., 2023; Tang et al., 2022), natural gamma-ray density (e.g., Huang and Hinnov, 2019; Sierro et al., 2000; Tang et al., 2022) and P-wave velocity (e.g., Sierro et al., 2000). We suggest that, if sonic or density logs can preserve orbitally forced climate signals, it is reasonable to expect that the same signals are expressed in the overall acoustic impedance.

5.2. *Expression of acoustic impedance cyclicity in seismic reflection data*

If cyclicity is preserved in the acoustic impedance, how and when can we image it in seismic reflection data? Consider that the preservation of orbital cyclicity in sedimentary strata is already an exceptional case, due to the filtering of the astronomical signal at all stages through the climate and depositional system (Section 5.1). Seismic cyclostratigraphy adds a further "filter" in the form of the geophysical constraints of the seismic reflection experiment (Section 2.1), plus any maximum limit on the vertical resolution imposed by the recording sampling interval. As such, should we consider that seismic cyclostratigraphy is likely to be widely applicable, in many depositional settings and with many typical seismic acquisitions, or is it likely to require specific geological conditions and specially designed geophysical experiments?

At a high level, the spatial frequency of the cyclicity needs to be within the bandwidth of the seismic source, and the variation in reflectivity caused by the cyclic signal needs to be strong enough to be reliably detectable above the noise floor of the seismic data (i.e., produce a distinct spectral peak). Real-world seismic reflection data are, however, recorded in TWTT (i.e., not in depth), and the frequency spectrum of both the signal and the noise is not flat and is non-stationary (Section 2.2). This means that the signal-to-noise level, and thus the discriminatory power to identify cyclicity, changes both with time and frequency. This motivates using a Monte Carlo synthetic modelling approach (as in this study) to determine, at least to a first order, the variation in statistical significance of seismic cyclostratigraphy for a given scenario and stratigraphic interval.

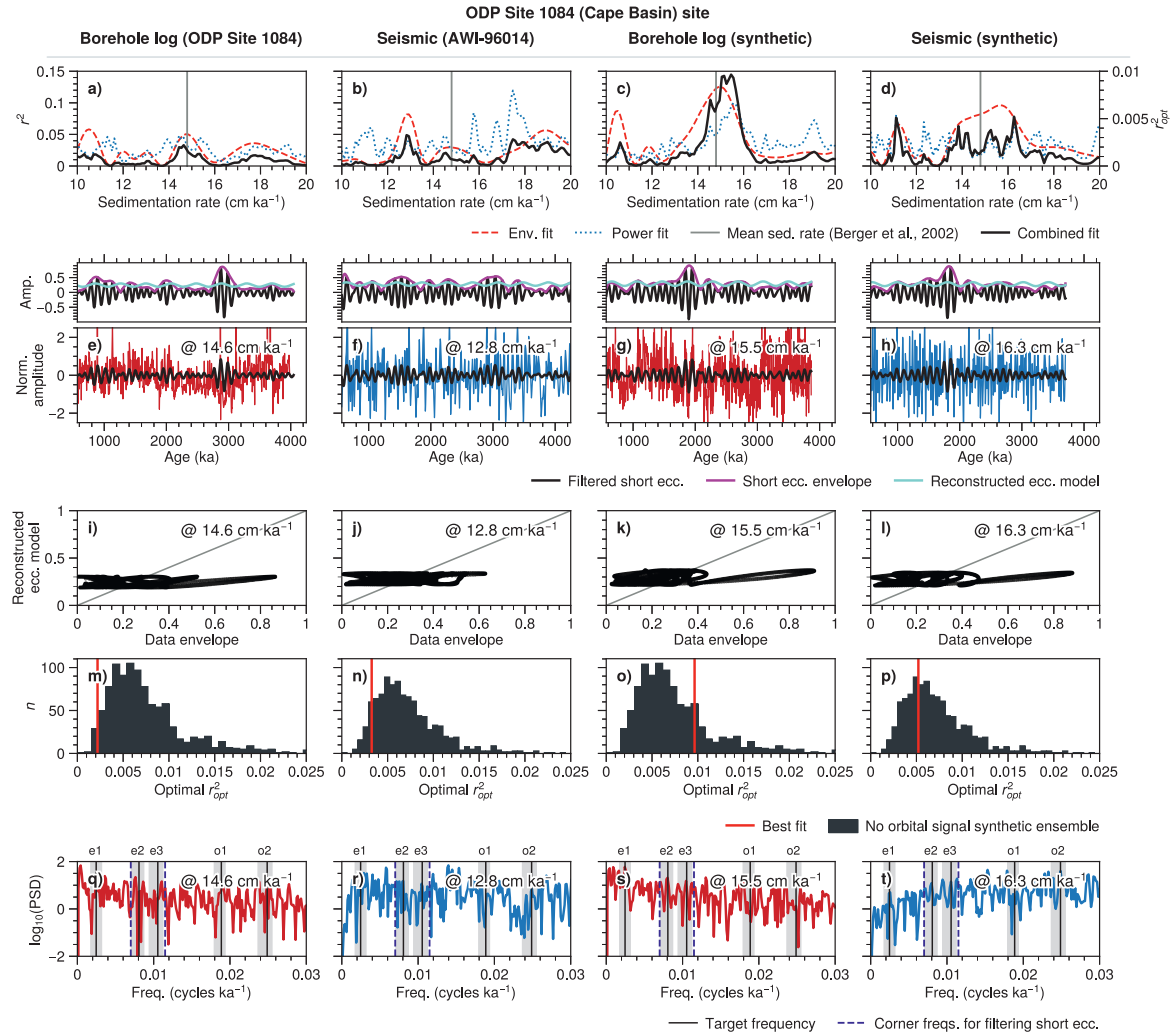

Fig. 10. Short-period eccentricity modulation analysis (TimeOpt) for both the borehole log and whitened seismic data for the ODP Site 1084 real-world data (first and second columns; Fig. 5) and one realisation of the synthetic model that includes an orbital signal (third and fourth columns; Fig. 7). Note that the first 100 m have not been considered to avoid including data from the ODP Site 1084 well casing. (a-d) Goodness-of-fit criteria for each candidate sedimentation rate. (e-h) Data scaled and stretched to age domain with the best fitting sedimentation rates, with comparison (above) between the envelope of the short-period eccentricity band and the reconstructed eccentricity model. (i-l) Crossplot of the fit between the data amplitude envelope and the reconstructed eccentricity model. (m-p) The optimal r^2_{opt} for this realisation compared to a histogram of r^2_{opt} values for the ensemble of simplified synthetic models that do not include an orbital signal. (q-t) Power spectra of the data in age domain with the dominant orbital periods shaded, and the TimeOpt target eccentricities and short-period eccentricity band indicated. Shaded zones represent the dominant eccentricity (e1 = 405 kyr, e2 = 125 kyr, e3 = 95 kyr) and obliquity (o1 = 56 kyr, o2 = 41 kyr) cycles for the interval 4.6 Ma–present.

The period of the orbital cyclicity, T (in kyr), can be related to the seismic wavelength, λ (in m), and the sedimentation rate, α (in cm ka^{-1}), by $T = 100\lambda/\alpha$. The seismic wavelength is related to the seismic velocity, v (in ms^{-1}), and the frequency, f (in Hz), by $\lambda = v/f$, meaning that $T = 100v/(\alpha f)$. Assuming constant seismic velocity and constant sedimentation rate within an interval, we can estimate the range of resolvable periodicities by using the minimum and maximum frequencies present in the seismic bandwidth. The maximum resolvable cycle length can be further constrained by supposing that we require, e.g., at least 10 full cycles preserved within an interval to make a distinct spectral peak. Hiatuses or event beds will reduce the amplitude of spectral peaks and contaminate the spectrum, reducing the statistical power (this also applies to traditional cyclostratigraphy from directly sampled data). An example of this phenomenon is the ODP Site 1084 (Cape Basin) borehole logging data, where diagenesis has caused "spikes" in the sonic and density logs (Fig. 5). Conversely, thicker sequences preserve more cycles, which will increase the statistical power of cyclostratigraphy. This implies that high-resolution data from areas with high sedimentation rates are best suited to seismic cyclostratigraphy since they image stratigraphic sequences that encompass many orbital cycles.

As an example, typical source frequencies for multi-channel seismic data are on the order of 10–100 Hz. For a shallow marine interval with average velocity 1600 ms^{-1} and an average sedimentation rate of 20 cm ka^{-1}, this means that the maximum range of resolvable cyclicity is from 80 to 800 kyr (i.e, 405 kyr, 125 kyr and 95 kyr eccentricity orbital cycles). If we assume that a minimum of 10 complete cycles are required to resolve a distinct spectral peak, this implies an interval of at least 1.01 s TWTT thickness (810 m or 4.05 Ma) is needed to image 405 kyr eccentricity cycles. More sophisticated analysis for estimating, e.g., the significance level of spectral peaks, would require a Monte Carlo ensemble analysis as performed in this study, which can also properly account for variations in sedimentation rate, source spectrum and seismic velocity.

Mitchell (2016) makes the case against seismic cyclostratigraphy for spectral analysis performed on sub-bottom profiler data (Horn and Uenzelmann-Neben, 2016). Sub-bottom profiler data operate at higher frequencies than the multi-channel airgun seismic data (e.g., Fig. 5), and thus their spectra are much more strongly affected by the frequency-

dependent attenuation induced by absorption. The point made is that the attenuation accumulated within a study interval is enough to distort the overall average spectrum over the interval so that identifying cycles would be impossible. It is, however, possible to quantify attenuation, with the seismic quality factor *Q*, using measurements from a vertical seismic profile (VSP) or by directly inverting surface seismic data (e.g., Dasgupta and Clark, 1998). The spectral distortion generated by absorption can by reversed during seismic processing by, for example, a *Q* compensation filter. Indeed, we could also include an attenuation compensation step in the spectral whitening (Section 2.2). Whether or not attenuation compensation is included, here we do model the effect of attenuation in the visco-acoustic seismic modelling, which allows us to include the effect of attenuation on the discriminatory power of seismic cyclostratigraphy hypothesis testing.

5.3. Limitations of statistical significance for cyclostratigraphy with seismic data

The spurious spectral peaks in Fig. 1d should be a warning that if we want to do seismic cyclostratigraphy we do need to properly consider the statistical significance of peaks (and the discriminatory power of the hypothesis testing method). Power spectra of seismic traces suffer from spurious peaks as do those of borehole logs, but the non-flat frequency response of the seismic wavelet means that spurious peaks may have relatively higher amplitude than in the power spectra of borehole logs when they fall close to the dominant frequency of the seismic wavelet (compare Figs. 1b and d). Hypothesis testing using confidence intervals to identify orbital forcing from seismic data suffers from the same caveats as for classical cyclostratigraphy from direct sampling methods (Smith, 2023; Vaughan et al., 2011; Weedon, 2022). Issues surrounding multiple frequency testing, "p-hacking", misuse of confidence intervals and subsequent effects on the expected false positive rates all still apply. We do not address these here, as with this study we primarily aim to compare the discriminatory power of borehole and seismic cyclostratigraphy.

5.4. Amplitude modulation and frequency bundling in seismic data

Eccentricity modulation and bundling analysis relies on the amplitude modulation of short period cycles (typically the precession band) on longer period cycles (typically the eccentricity band) and the predictable frequency ratio (bundling) between spectral peaks (Zeeden et al., 2015). In this study we apply TimeOpt (Meyers, 2015) to tune both the borehole log and seismic data using short-period eccentricity analysis, i.e., using the modulation of 125 kyr and 95 kyr cycles by the 405 kyr long-period eccentricity cycle (Section 2.5).

TimeOpt analysis uses the envelope of the filtered carrier frequency to reconstruct the modulator frequency. This will inevitably be more difficult for seismic data compared to directly sampled data (e.g., a borehole log) due to the non-flat frequency response of seismic data. If the modulator frequency falls outside the seismic bandwidth, then amplitude modulation will not be imaged by the carrier band. TimeOpt, however, also simultaneously inverts for the best fit according to the intensity of predicted target spectral peaks ("frequency bundling", Meyers, 2015). This provides a second measure, independent of the modulation analyis, to invert for the sedimentation rate. Note that neither the amplitude modulation nor the bundling analysis require that statistically significant spectral peaks are preserved, the significance of the TimeOpt result is instead quantified by comparing the peak goodness of fit to the distribution of the peak goodness of fit of an ensemble of "noise" models that do not contain an anstronomical signal. Here we demonstrate this using the visco-acoustic seismic modelling to generate a comparable noise ensemble (Figs. 4g,h and 10m-p).

We recover a good estimation of the sedimentation rate directly from the seismic data for the simplified synthetic (Section 3.3; Fig. 4), but more mixed results for the ODP Site 1084 real-world data and synthetic models (Section 4.5; Fig. 10). This is likely due to the variable sedimentation rate at ODP Site 1084, and could also be due to extra noise (including multiples) and the different sensitivity within the seismic bandwidth between the simplified synthetic model and the ODP Site 1084 real data and model. Future studies should examine TimeOpt optimization using variable sedimentation rate templates (Meyers, 2015, 2019) to seismic data. More synthetic modelling and real-world data case studies are needed to establish if TimeOpt-style amplitude modulation and/or frequency bundling approaches can be widely applied to the seismic case.

5.5. Potential applications of seismic cyclostratigraphy

One potential application of seismic cyclostratigraphy is to extrapolate laterally away from boreholes where there is already an established cyclostratigraphic correlation with a seismically-relevant borehole log. By assuming that orbital cyclicity seen in the seismic data at the borehole location will also be seen in the same stratigraphic interval at a distance from the borehole, we can invert for variation in the sedimentation rate by tuning the age model laterally. In other words, if seismic stratigraphy is typically used to extrapolate chrono-stratigraphic horizons away from the borehole, seismic cyclostratigraphy may allow the derivation and extrapolation of variable-rate age models between important stratigraphic horizons. Similar extrapolation could also be performed vertically, either beneath the maximum penetration depth of the borehole or interpolating across intervals which suffered from poor core recovery or washing. This would allow the extension of borehole-derived age models to undrilled or uncored depths.

Direct application to seismic data without an *a priori* calibration with borehole cyclostratigraphy may also be possible, where the relevant orbital terms of interest fall within the seismic bandwidth. For example, for attempting to drill expanded intervals for paleoclimate research, being able to infer the likely number of preserved orbital cycles from the seismic before drilling could be useful to predict, e.g., plausible sedimentation rates. In addition, positive indication of seismic cyclicity implies that there should also be a cyclostratigraphy preserved in the sediment physical properties and likely also in more traditional directly sampled parameters such as geochemical and biostratigraphic proxies. For proposed drill sites where establishing an orbitally-tuned stratigraphic age model is important, seismic cyclostratigraphy could be a useful screening tool based on seismic site survey data.

Despite generally being lower resolution and more noisy (therefore having lower discriminatory power to resolve cyclicity), seismic cyclostratigraphy may also present some advantages over traditional, directly sampled cyclostratigraphy. Compared to drill core, there is no core loss, decompaction, washing, drilling-related disturbance or splicing issues. Compared to borehole logs, there are no problems with depth synchronisation or the borehole condition. Seismic data represents a non-destructive, remote method to investigate cyclostratigraphy, and something closer to an *in situ* view of the subsurface, presumably representing a more continuous and less distorted paleoclimate record. Outcrop examples can suffer from limited exposure, whereas seismic data generally have good lateral coverage and a depth penetration of several kilometres below the seafloor, so there is potential to investigate longer intervals which may reveal, for example, very long eccentricity modulation cycles (Hinnov, 2000). There is also the possibility to stack seismic traces laterally to improve the signal-to-noise ratio beyond using a single trace (as in this study).

5.6. Wider potential for cyclostratigraphy with geophysical reflection data

In this study we investigate using marine multi-channel seismic reflection data to image orbital cyclicity, and attempt to calibrate confidence levels using Monte Carlo ensemble modelling. Similar principles could also be applied to other geophysical reflection techniques, such as sub-bottom profilers. Horn and Uenzelmann-Neben (2016) identify

orbital cyclicity (obliquity and precession cycles) from sub-bottom profiler records offshore New Zealand. Sub-bottom profilers differ from conventional multi-channel marine seismic reflection data in two key ways: they typically record only a single channel of data, and they use a higher frequency band than multi-channel seismics (typically 1–10 kHz, compared to 10–100 Hz). The single channel means that the noise level is higher, as traces in the image are not stacked. The higher frequency range means that there is strong frequency-dependent attenuation, which limits signal penetration and presumably will reduce the amplitude of spectral peaks above the noise floor, particularly at high frequencies (Mitchell, 2016). Sub-bottom profiler data could, however, offer several potential advantages over multi-channel seismic data. As it can resolve much higher frequencies, on a scale much closer to core-scale, perhaps we could resolve shorter periodicity orbital cyclicity, such as 18–25 kyr precession cycles. As the source is parametric and generated by an electrical transducer, we often have a much better approximation of the frequency content of the source wavelet compared to airgun sources. It should be noted that it is important to use the raw trace data (not the envelope, as is commonly displayed and recorded) to be able to derive meaningful power spectra.

With any kind of geophysical reflection data, the resolvability of different orbital cycles depends primarily on the temporal resolution (source bandwidth) and the depth of investigation, in addition to secondary problems surrounding the non-stationary wavelet, internal multiples and higher noise floor (Section 2.1). We suggest, therefore, to first perform a basic assessment using the 'rules-of-thumb' outlined in Section 5.2, before performing a more thorough analysis of the discriminatory power for example using Monte Carlo ensemble modelling, as shown in this study.

6. Conclusions

If orbital cyclicity is preserved in the acoustic impedance, and if after stretching from TWTT to stratigraphic age domain the orbital periodicity in question falls within the bandwidth of the seismic image, we may be able to image the cyclicity as distinct peaks in the power spectrum of the seismic trace. The narrow-band nature of active source seismic data, plus the loss of long-wavelength acoustic impedance information during reflection imaging, and extra noise introduced by the seismic experiment means that an alternative spectral whitening procedure is required. Resulting spectral peaks will be lower amplitude and the background noise floor will be higher than for a comparable power spectral analysis based on a borehole log. In general, this means that seismic cyclostratigraphy will have lower statistical power and a higher false detection rate than a comparable borehole cyclostratigraphy (Figs. 3 and 9).

The sedimentary environment that is most promising for the detection of orbital cyclicity in seismic reflection images is that of sediment drifts, that typically host a continuous, relatively expanded sedimentary record in which climatically-modulated changes in physical properties should be reflected in the acoustic impedance. The sediment accumulation rate in such sedimentary sequences is typically not constant, but changes are gradual and can be accounted for with a borehole-derived age model.

Our Monte Carlo ensemble modelling experiments indicate that, after spectral whitening, seismic reflection traces can resolve orbital cyclicity as distinct peaks in the power spectrum under realistic geological and geophysical conditions (Fig. 2). For some orbital periods, the discriminatory power can be close to a comparable borehole cyclostratigrapy, however this is strongly frequency-dependent within the seismic bandwidth, and the discriminatory power is always lower than a comparable borehole spectral analysis (Fig. 3). The Monte Carlo ensemble modelling based on the ODP Site 1084 (Cape Basin) scenario shows that for some orbital periods (41 kyr), the statistical power might be similar to a comparable borehole cyclostratigraphy. In general, however, we see a very high false positive rate for most orbital periods. Nevertheless, the spectral peaks likely do represent cyclicity, as we have a correlated borehole in which there is existing evidence of preservation of orbital forcing (Berger et al., 2002). The false positive rate is so high, however, that orbital cyclicity cannot be inferred from the seismic data alone, without other evidence of cyclicity.

In general, we can say that hypothesis testing for orbital cyclicity from seismic reflection data is possible under some typical geological and geophysical conditions. Calibration of confidence levels is tricky due to the strong frequency-dependence of the sensitivity and specificity, we recommend that this kind of ensemble modelling is performed before attempting seismic cyclostratigraphy, at least to understand whether it is feasible for a given scenario and for the targetted orbital periodicities. Seismic cyclostratigraphy offers promising applications for extrapolating away from boreholes with an already established cyclostratigraphic framework (preserved in the acoustic impedance). Moreover, there is potential to investigate very long cycles with this non-destructive method that uses data representative of *in situ* conditions, without core loss, decompaction and disturbance issues associated with drilling and logging.

Open research section

The seismic profile AWI-96014 is available at Uenzelmann-Neben and Weigelt (2023). Borehole logs and the age model for ODP Site 1084 are available from https://mlp.ldeo.columbia.edu/data/odp/leg175/1084A/ and Wefer et al. (2002). The TimeOpt demonstrations were run using the open source R package astrochron (Meyers, 2014). Code to generate all figures in this article will be archived and made publically available at Ford (2024) on acceptance of this article.

Declaration of competing interest

The authors declare that they have no known competing financial interests or personal relationships that could have appeared to influence the work reported in this paper.

Data availability

Data used in this article are all publicly available. Code to generate all figures in this article will be archived and made publicly available at on acceptance of this article.

Acknowledgements

This work used data provided by the Ocean Drilling Project (ODP). The research was supported by the ECORD Science Support and Advisory Committee (ESSAC) Office at OGS. We thank Christian Zeeden and an anonymous reviewer for thorough and constructive reviews that significantly improved the manuscript. Christopher Fielding is thanked for comments as handling editor.

References

Abdi, H., 2007. The Bonferonni and Šidák corrections for multiple comparisons. In: Salkind, N. (Ed.), Encyclopedia of Measurement and Statistics. Sage, Thousand Oaks (CA).

Berger, W.H., 2012. Miklankovitch Theory - Hits and Misses. Technical Report. Scripps Institution of Oceanography.

Berger, W.H., Lange, C.B., Wefer, G., 2002. Upwelling history of the Benguela-Namibia system: a synthesis of Leg 175 results. In: Wefer, G., Berger, W., Richter, C. (Eds.), Proceedings of the Ocean Drilling Program, Scientific results. Ocean Drilling Program. Volume 175 of Proceedings of the Ocean Drilling Program, pp. 1–103. https://doi.org/10.2973/odp.proc.sr.175.2002.

Blondel, S., Ford, J., Lockwood, A., Del Ben, A., Camerlenghi, A., 2023. Reprocessing 2-D airgun seismic reflection data SALTFLU (salt deformation and sub-salt fluid circulation in the Algero-Balearic abyssal plain) in the Balearic promontory and the Algerian basin. Mar. Geophys. Res. 44, 13. https://doi.org/10.1007/s11001-023-09512-5.

Carcione, J.M., 2014. Wave Fields in Real Media: Wave Propagation in Anisotropic, Anelastic, Porous and Electromagnetic Media. Elsevier.

Castagna, J.P., Batzle, M.L., Eastwood, R.L., 1985. Relationships between compressional-wave and shear-wave velocities in clastic silicate rocks. GEOPHYSICS 50, 571–581. https://doi.org/10.1190/1.1441933.
Claerbout, J.F., 1985. Imaging the Earth's Interior. Blackwell Scientific Publications.
Dasgupta, R., Clark, R.A., 1998. Estimation of Q from surface seismic reflection data. Geophysics 63, 2120–2128. https://doi.org/10.1190/1.1444505.
Diester-Haass, L., Meyers, P.A., Bickert, T., 2004. Carbonate crash and biogenic bloom in the late Miocene: Evidence from ODP Sites 1085, 1086, and 1087 in the Cape Basin, Southeast Atlantic Ocean. Paleoceanography 19. https://doi.org/10.1029/2003PA000933.
Ford, J., 2024. Code to reproduce results of Ford et. al. "Seismic cyclostratigraphy: Hypothesis testing for orbital cyclicity using seismic reflection data" https://doi.org/10.5281/zenodo.10640647.
Gardner, G.H.F., Gardner, L.W., Gregory, A.R., 1974. Formation velocity and density—the diagnostic basics for stratigraphic traps. GEOPHYSICS 39, 770–780. https://doi.org/10.1190/1.1440465.
Grützner, J., Rebesco, M., Cooper, A., Forsberg, C., Kryc, K., Wefer, G., 2003. Evidence for orbitally controlled size variations of the East Antarctic Ice Sheet during the late Miocene. Geology 31, 777–780. https://doi.org/10.1130/G19574.1.
Hall, P.L., Astill, D.M., McConnell, J.D.C., 1986. Thermodynamic and structural aspects of the dehydration of smectites in sedimentary rocks. Clay Miner. 21, 633–648. https://doi.org/10.1180/claymin.1986.021.4.13.
Hays, J.D., Imbrie, J., Shackleton, N.J., 1976. Variations in the Earth's Orbit: Pacemaker of the Ice Ages. Science 194, 1121–1132. https://doi.org/10.1126/science.194.4270.1121.
Hepp, D.A., Mörz, T., Grützner, J., 2006. Pliocene glacial cyclicity in a deep-sea sediment drift (Antarctic Peninsula Pacific margin). Palaeogeogr. Palaeoclimatol. Palaeoecol. 231, 181–198. https://doi.org/10.1016/j.palaeo.2005.07.030.
Hernández-Molina, F.J., Sierro, F.J., Llave, E., Roque, C., Stow, D.A.V., Williams, T., Lofi, J., Van der Schee, M., Arnáiz, A., Ledesma, S., Rosales, C., Rodríguez-Tovar, F. J., Pardo-Igúzquiza, E., Brackenridge, R.E., 2016. Evolution of the Gulf of Cadiz margin and Southwest Portugal contourite depositional system: Tectonic, sedimentary and paleoceanographic implications from IODP Expedition 339. Mar. Geol. 377, 7–39. https://doi.org/10.1016/j.margeo.2015.09.013.
Hilgen, F.J., Hinnov, L.A., Abdul Aziz, H., Abels, H.A., Batenburg, S., Bosmans, J.H.C., de Boer, B., Hüsing, S.K., Kuiper, K.F., Lourens, L.J., Rivera, T., Tuenter, E., Van de Wal, R.S.W., Wotzlaw, J.F., Zeeden, C., 2015. Stratigraphic continuity and fragmentary sedimentation: the success of cyclostratigraphy as part of integrated stratigraphy. Geol. Soc. Lond. Spec. Publ. 404, 157–197. https://doi.org/10.1144/SP404.12.
Hillenbrand, C.D., Fütterer, D.K., 2002. Neogene to Quaternary deposition of opal on the continental rise West of the Antarctic Peninsula, ODP Leg 178, Sites 1095, 1096, and 1101. In: Barker, P., Camerlenghi, A., Acton, G., Ramsay, A. (Eds.), Proceedings of the Ocean Drilling Program, Scientific Results. https://doi.org/10.2973/odp.proc.sr.178.215.2001.
Hinnov, L.A., 2000. New perspectives on orbitally forced stratigraphy. Annu. Rev. Earth Planet. Sci. 28, 419–475. https://doi.org/10.1146/annurev.earth.28.1.419.
Hinnov, L.A., 2013. Cyclostratigraphy and its revolutionizing applications in the earth and planetary sciences. GSA Bull. 125, 1703–1734. https://doi.org/10.1130/B30934.1.
Holliger, K., 1996. Upper-crustal seismic velocity heterogeneity as derived from a variety of *P* -wave sonic logs. Geophys. J. Int. 125, 813–829. https://doi.org/10.1111/j.1365-246X.1996.tb06025.x.
Horn, M., Uenzelmann-Neben, G., 2016. The spatial extent of the Deep Western Boundary Current into the Bounty Trough: New evidence from Parasound sub-bottom profiling. Mar. Geophys. Res. 37, 145–158. https://doi.org/10.1007/s11001-016-9268-1.
Huang, C., Hinnov, L., 2019. Astronomically forced climate evolution in a saline lake record of the middle Eocene to Oligocene, Jianghan Basin, China. Earth Planet. Sci. Lett. 528, 115846. https://doi.org/10.1016/j.epsl.2019.115846.
Huybers, P., Wunsch, C., 2005. Obliquity pacing of the late Pleistocene glacial terminations. Nature 434, 491–494. https://doi.org/10.1038/nature03401.
Irving, J., Holliger, K., 2010. Geostatistical inversion of seismic and ground-penetrating radar reflection images: what can we actually resolve? Geophys. Res. Lett. 37. https://doi.org/10.1029/2010GL044852.
Jowett, E.C., Iii, L.M.C., Davis, B.W., 1993. Predicting Depths of Gypsum Dehydration in Evaporitic Sedimentary Basins. AAPG Bull. 77, 402–413.
Laskar, J., Robutel, P., Joutel, F., Gastineau, M., Correia, A.C.M., Levrard, B., 2004. A long-term numerical solution for the insolation quantities of the Earth. Astron. Astrophys. 428, 261–285. https://doi.org/10.1051/0004-6361:20041335.
Levander, A., Hobbs, R.W., Smith, S.K., England, R.W., Snyder, D.B., Holliger, K., 1994. The crust as a heterogeneous "optical" medium, or "crocodiles in the mist". Tectonophysics 232, 281–297. https://doi.org/10.1016/0040-1951(94)90090-6.
Liu, S., Feng, A., Yang, L., Du, J., Yu, Y., Feng, W., Wang, Y.P., 2020. Stratigraphic and three-dimensional morphological evolution of the late Quaternary sequences in the western Bohai Sea, China: Controls related to eustasy, high sediment supplies and neotectonics. Mar. Geol. 427, 106246. https://doi.org/10.1016/j.margeo.2020.106246.
Llave, E., Hernández-Molina, F., Somoza, L., Díaz-del-Río, V., Stow, D., Maestro, A., Alveirinho Dias, J., 2001. Seismic stacking pattern of the Faro-Albufeira contourite system (Gulf of Cadiz): a Quaternary record of paleoceanographic and tectonic influences. Mar. Geophys. Res. 22, 487–508. https://doi.org/10.1023/A:1016355801344.
Llave, E., Hernández-Molina, F.J., García, M., Ercilla, G., Roque, C., Juan, C., Mena, A., Preu, B., Van Rooij, D., Rebesco, M., Brackenridge, R., Jané, G., Gómez-Ballesteros, M., Stow, D., 2020. Contourites along the Iberian continental margins: Conceptual and economic implications. Geol. Soc. Lond. Spec. Publ. 476, 403–436. https://doi.org/10.1144/SP476-2017-46.
Louboutin, M., Lange, M., Luporini, F., Kukreja, N., Witte, P.A., Herrmann, F.J., Velesko, P., Gorman, G.J., 2019. Devito (v3.1.0): an embedded domain-specific language for finite differences and geophysical exploration. Geosci. Model Dev. 12, 1165–1187. https://doi.org/10.5194/gmd-12-1165-2019.
Mann, M.E., Lees, J.M., 1996. Robust estimation of background noise and signal detection in climatic time series. Clim. Chang. 33, 409–445. https://doi.org/10.1007/BF00142586.
Mavko, G., Kjartansson, E., Winkler, K., 1979. Seismic wave attenuation in rocks. Rev. Geophys. 17, 1155–1164. https://doi.org/10.1029/RG017i006p01155.
Mavko, G., Mukerji, T., Dvorkin, J., 2009. The Rock Physics Handbook: Tools for Seismic Analysis of Porous Media. Cambridge University Press.
Meyers, S.R., 2012. Seeing red in cyclic stratigraphy: Spectral noise estimation for astrochronology. Paleoceanography 27. https://doi.org/10.1029/2012PA002307.
Meyers, S.R., 2014. Astrochron: An R Package for Astrochronology. URL: https://cran.r-project.org/package=astrochron.
Meyers, S.R., 2015. The evaluation of eccentricity-related amplitude modulation and bundling in paleoclimate data: an inverse approach for astrochronologic testing and time scale optimization. Paleoceanography 30, 1625–1640. https://doi.org/10.1002/2015PA002850.
Meyers, S.R., 2019. Cyclostratigraphy and the problem of astrochronologic testing. Earth Sci. Rev. 190, 190–223. https://doi.org/10.1016/j.earscirev.2018.11.015.
Meyers, S.R., Malinverno, A., 2018. Proterozoic Milankovitch cycles and the history of the solar system. Proc. Natl. Acad. Sci. 115, 6363–6368. https://doi.org/10.1073/pnas.1717689115.
Meyers, S.R., Sageman, B.B., 2007. Quantification of deep-time orbital forcing by average spectral misfit. Am. J. Sci. 307, 773–792. https://doi.org/10.2475/05.2007.01.
Mitchell, N.C., 2016. Comment on: "The spatial extent of the Deep Western Boundary Current into the Bounty Trough: New evidence from Parasound sub-bottom profiling" by Horn and Uenzelmann-Neben. Mar. Geophys. Res. 37, 371–374. https://doi.org/10.1007/s11001-016-9287-y.
Moore, C.H., 1989. Carbonate Diagenesis and Porosity. Elsevier.
Ocean Drilling Program, 2004. Overview of Logging Tools: Measurements, Units and Acronyms. Technical report 1. URL: http://www.odplegacy.org/PDF/Operations/Engineering/Logging_Tools/Acronyms_Overview.pdf.
Poppeliers, C., 2007. Estimating vertical stochastic scale parameters from seismic reflection data: Deconvolution with non-white reflectivity. Geophys. J. Int. 168, 769–778. https://doi.org/10.1111/j.1365-246X.2006.03239.x.
Prieto, G.A., 2022. The multitaper spectrum analysis package in Python. Seismol. Res. Lett. 93, 1922–1929. https://doi.org/10.1785/0220210332.
Pullammanappallil, S., Levander, A., Larkin, S.P., 1997. Estimation of crustal stochastic parameters from seismic exploration data. J. Geophys. Res. Solid Earth 102, 15269–15286. https://doi.org/10.1029/97JB01144.
Pytte, A.M., Reynolds, R.C., 1989. The thermal transformation of Smectite to Illite. In: Naeser, N.D., McCulloh, T.H. (Eds.), Thermal History of Sedimentary Basins. Springer, New York, NY, pp. 133–140. https://doi.org/10.1007/978-1-4612-3492-0_8.
Rebesco, M., Camerlenghi, A., Munari, V., Mosetti, R., Ford, J., Micallef, A., Facchin, L., 2021. Bottom current-controlled Quaternary sedimentation at the foot of the Malta Escarpment (Ionian Basin, Mediterranean). Mar. Geol. 441, 106596. https://doi.org/10.1016/j.margeo.2021.106596.
Schulz, M., Mudelsee, M., 2002. REDFIT: estimating red-noise spectra directly from unevenly spaced paleoclimatic time series. Comput. Geosci. 28, 421–426. https://doi.org/10.1016/S0098-3004(01)00044-9.
Sheriff, R.E., Geldart, L.P., 1995. Exploration Seismology. Cambridge University Press.
Shipboard Scientific Party, 1998a. Explanatory notes. In: Wefer, G., Berger, W., Richter, C., Shipboard Scientific Party (Eds.), Proc. ODP, Init. Repts, vol. 175. Ocean Drilling Program, College Station, TX. https://doi.org/10.2973/odp.proc.ir.175.102.1998.
Shipboard Scientific Party, 1998b. Introduction: Background, scientific objectives, and principal results for Leg 175 (Benguela Current and Angola-Benguela upwelling systems). In: Wefer, G., Berger, W., Richter, C., Shipboard Scientific Party (Eds.), Proc. ODP, Init. Repts, vol. 175. Ocean Drilling Program, College Station, TX. https://doi.org/10.2973/odp.proc.ir.175.101.1998.
Shipboard Scientific Party, 1998c. Site 1084. In: Wefer, G., Berger, W., Richter, C., Shipboard Scientific Party (Eds.), Proc. ODP, Init. Repts, vol. 175. Ocean Drilling Program, College Station, TX. https://doi.org/10.2973/odp.proc.ir.175.112.1998.
Sierro, F.J., Ledesma, S., Flores, J.A., Torrescusa, S., del Olmo, W.M., 2000. Sonic and gamma-ray astrochronology: Cycle to cycle calibration of Atlantic climatic records to Mediterranean sapropels and astronomical oscillations. Geology 28, 695–698. https://doi.org/10.1130/0091-7613(2000)28<695:SAGACT>2.0.CO;2.
Smith, D.G., 2023. The Orbital Cycle Factory: sixty cyclostratigraphic spectra in need of re-evaluation. Palaeogeogr. Palaeoclimatol. Palaeoecol. 628, 111744. https://doi.org/10.1016/j.palaeo.2023.111744.
Sproson, A.D., 2020. Pacing of the latest Ordovician and Silurian carbon cycle by a ~4.5 Myr orbital cycle. Palaeogeogr. Palaeoclimatol. Palaeoecol. 540, 109543. https://doi.org/10.1016/j.palaeo.2019.109543.
Stow, D.A., Faugères, J.C., Viana, A., Gonthier, E., 1998. Fossil contourites: a critical review. Sediment. Geol. 115, 3–31. https://doi.org/10.1016/S0037-0738(97)00085-7.
Stow, D.A.V., Faugères, J.C., Howe, J.A., Pudsey, C.J., Viana, A.R., 2002. Bottom currents, contourites and deep-sea sediment drifts: current state-of-the-art. Geol. Soc. Lond. Mem. 22, 7–20. https://doi.org/10.1144/GSL.MEM.2002.022.01.02.

Tang, Y., Zheng, M., Wang, X., Wang, T., Cheng, H., Hei, C., 2022. The floating astronomical time scale for the terrestrial early Permian Fengcheng Formation from the Junggar Basin and its stratigraphic and palaeoclimate implications. Geol. J. 57, 4842–4856. https://doi.org/10.1002/gj.4575.

Thomson, D., 1982. Spectrum estimation and harmonic analysis. Proc. IEEE 70, 1055–1096. https://doi.org/10.1109/PROC.1982.12433.

Uenzelmann-Neben, G., Weigelt, E., 2023. Cape Basin, Seismic Profile AWI-96014. https://doi.org/10.1594/PANGAEA.958791.

Vandorpe, T.P., Van Rooij, D., Stow, D.A.V., Henriet, J.P., 2011. Pliocene to recent shallow-water contourite deposits on the shelf and shelf edge off south-western Mallorca, Spain. Geo-Mar. Lett. 31, 391–403. https://doi.org/10.1007/s00367-011-0248-9.

Varela, C.L., Rosa, A.L.R., Ulrych, T.J., 1993. Modeling of attenuation and dispersion. Geophysics 58, 1167–1173. https://doi.org/10.1190/1.1443500.

Vaughan, S., Bailey, R.J., Smith, D.G., 2011. Detecting cycles in stratigraphic data: Spectral analysis in the presence of red noise. Paleoceanography 26. https://doi.org/10.1029/2011PA002195.

Vaughan, S., Bailey, R.J., Smith, D.G., 2015. Cyclostratigraphy: Data filtering as a source of spurious spectral peaks. Geol. Soc. Lond. Spec. Publ. 404, 151–156. https://doi.org/10.1144/SP404.11.

Volpi, V., Camerlenghi, A., Hillenbrand, C.D., Rebesco, M., Ivaldi, R., 2003. Effects of biogenic silica on sediment compaction and slope stability on the Pacific margin of the Antarctic Peninsula. Basin Res. 15, 339–363. https://doi.org/10.1046/j.1365-2117.2003.00210.x.

Weedon, G.P., 2003. Time-Series Analysis and Cyclostratigraphy: Examining Stratigraphic Records of Environmental Cycles. Cambridge University Press.

Weedon, G.P., 2022. Problems with the current practice of spectral analysis in cyclostratigraphy: avoiding false detection of regular cyclicity. Earth Sci. Rev. 235, 104261. https://doi.org/10.1016/j.earscirev.2022.104261.

Wefer, G., Berger, W., Richter, C., 2002. Proceedings of the Ocean Drilling Program, 175 Scientific Results. Volume 175 of Proceedings of the Ocean Drilling Program. Ocean Drilling Program. https://doi.org/10.2973/odp.proc.sr.175.2002.

Weigelt, E., Uenzelmann-Neben, G., 2007. Orbital forced cyclicity of reflector strength in the seismic records of the Cape Basin. Geophys. Res. Lett. 34. https://doi.org/10.1029/2006GL028376.

Zeeden, C., Meyers, S.R., Lourens, L.J., Hilgen, F.J., 2015. Testing astronomically tuned age models. Paleoceanography 30, 369–383. https://doi.org/10.1002/2014PA002762.

Zeeden, C., Ulfers, A., Pierdominici, S., Abadi, M.S., Vinnepand, M., Grelle, T., Hesse, K., Leu, K., Wonik, T., 2023. Downhole logging data for time series analysis and cyclostratigraphy. Earth Sci. Rev. 104436. https://doi.org/10.1016/j.earscirev.2023.104436.